Construction and Building Materials

Mechanical and fracture properties of sugar beetroot-based nanosheets (SNS) doped cementitious composites

--Manuscript Draft--

Manuscript Number:	CONBUILDMAT-D-22-11953R3
Article Type:	Research Paper
Keywords:	Bio-nanoplatelets; Cementitious Composites; Mechanical properties; Fracture properties
Corresponding Author:	Bo Huang, PhD Hunan University of Science and Technology Xiangtan, CHINA
First Author:	Bo Huang, PhD
Order of Authors:	Bo Huang, PhD
	Yin Chi, PhD
	Jianqun Wang, PhD
	Gongxun Wang, PhD
	Junjie Ye, PhD
	Eric Whale
	David Hepworth
	Jianqiao Ye, PhD
	Mohamed Saafi, PhD
Abstract:	This paper examines the mechanical and fracture properties of cementitious composites infused with a new type of 2D bio-nanoplatelets sheets, synthesized from sugar beet pulp waste. The sugar beetroot nanosheets (SNS) were added to the cement pastes at different concentrations. The influence of SNS treatment and water-to-cement (w/c) ratio on the performance of the cementitious composites was elucidated. The experimental results showed that 0.2-wt% and 0.35 were the optimal SNS concentration and w/c ratio for increasing the compressive, splitting tensile and flexural strength, flexural modulus, fracture energy and fracture toughness. These properties were enhanced by as much as 12.15%, 36.87%, 39.91%, 32.69%, 69.01% and 49.06%, respectively. This enhancement was due to crack deflection and crack bridging mechanisms in the cementitious composites as a result of the high specific surface area of SNS and the strong chemical and physical bonding of SNS with the hydration phases. The SNS materials offers strong advantages over graphene-based materials on improving the engineering properties of cementitious materials and reducing their cost and CO2 emissions.
Suggested Reviewers:	Hailong Ye, Ph.D. Assistant Professor, The University of Hong Kong hlye@hku.hk Dr. Hailong Ye is an Assistant Professor in the Department of Civil Engineering at The University of Hong Kong. He received his Ph.D. (2016) in Construction Materials from The Pennsylvania State University, USA. He worked as a Marie Curie Fellow at The University of Sheffield for a few months, before joining The University of Hong Kong in 2018. He is a Licensed Structural Engineer in China and a member of RILEM, American Concrete Institute (ACI), and American Ceramic Society (ACerS). He serves as an Associate Editor of ASCE's Journal of Materials in Civil Engineering. Dr. Ye's research interest includes Low-Carbon Cement Chemistry, Geopolymer and Alkali-Activated Concrete, Microbially Induced Concrete Corrosion (MICC), and Corrosion of Marine Concrete Structures. His research has been recognized by the 2020 Natural Science Award from the Ministry of Education of China.
	Rui Yu, Ph.D. Professor, Wuhan University of Technology

	r.yu@whut.edu.cn Rui Yu main research areas are as follows 1. Ultra-high performance fiber-reinforced composites 2. Marine functional building materials 3. Nano functional building materials 4. Construction waste recycled materials and ecological building materials
	Jianping Zhu, Ph.D. Professor, Henan Polytechnic University jianpingzhu@hpu.edu.cn Jianping Zhu has been engaged in the research of cement-based materials for a long time, especially in the research of solid waste resource utilization, nano-modified cement-based materials, particle size control cement-based materials, and concrete durability.
	Qingliang Yu, Ph.D. Associate Professor, Eindhoven University of Technology q.yu.1@tue.nl Qingliang Yu research interests primarily concern cement-bound materials, from materials to structural behavior understanding, covering micro-, meso- and macrolevel. His current research topics include functional building materials with air purifying, self-cleaning, or (ultra)high performance, concerning sustainability including alternative binders design like alkali-activated binder and application of industrial by-products or waste materials and durability under different exposure environment. His research follows the complete chain of knowledge from materials at molecular level to structural element, applying both experimental and modelling approaches. The current portfolio is well supported by his unique educational background from Civil Engineering to Materials Science.
	Shangtong Yang, Ph.D. Senior Lecturer, University of Strathclyde shangtong.yang@strath.ac.uk Shangtong Yang research interest is focused on the understanding of basic principles that control the mechanical properties and behaviours of civil engineering materials, in particular, rock-like materials such as concrete and rock. Under a variety/combination of loads and environemnts, the mechanical response of these materials is still a challenging topic. I look at the fundemental questions in developing rational constitutive models and the engineering applications to creating novel solution and technology.

Dear Editor:

We are submitting our revised manuscript titled "Mechanical and fracture properties of sugar beetroot-based nanosheets (SNS) doped cementitious composites" for review and publication in 'Construction and Building Materials'.

We declare that this manuscript is original that has not been published before and is not currently being considered for publication elsewhere. We confirm that the manuscript has been read and approved by all named authors and that there are no other persons who satisfied the criteria for authorship but are not listed. And the order of authors listed in the manuscript has been approved by all of us.

Thank you very much for your time and consideration.

Kind regards,

Dr. Bo Huang on behalf of all authors

School of Civil Engineering,

Hunan University of Science and Technology,

Xiangtan, 411201,

China

Email: Bohuang@hnust.edu.cn

Tel: +86-13187229766

Mechanical and fracture properties of sugar beetroot-based nanosheets (SNS) doped cementitious composites

Bo Huang [a,b], Yin Chi [c*], Jianqun Wang [a], Gongxun Wang [a], Junjie Ye [d], Eric Whale [e], David Hepworth [e], Jianqiao Ye [b], Mohamed Saafi [b*]

[a] School of Civil Engineering, Hunan University of Science and Technology, Xiangtan, 411201, China
[b] Department of Engineering, Lancaster University, Lancaster LA1 4YW, UK
[c] School of Civil Engineering, Wuhan University, Wuhan, 430072, China
[d] Research Center for Applied Mechanics, Key Laboratory of Ministry of Education for Electronic Equipment Structure Design, Xidian University, Xi'an 710071, China
[e] Cellucomp Ltd, Burntisland, Fife KY3 9DW, UK

Abstract

This paper examines the mechanical and fracture properties of cementitious composites doped with a new type of 2D bio-nanoplatelets sheets, synthesized from sugar beet pulp waste. The sugar beetroot nanosheets (SNS) were added to the cement pastes at different concentrations. The influence of SNS treatment and water-to-cement (w/c) ratio on the performance of the cementitious composites was elucidated. The experimental results showed that 0.2-wt% and 0.35 were the optimal SNS concentration and w/c ratio for increasing the compressive, splitting tensile and flexural strength, flexural modulus, fracture energy and fracture toughness. These properties were enhanced by as much as 12.15%, 36.87%, 39.91%, 32.69%, 69.01% and 49.06%, respectively. This enhancement was due to crack deflection and crack bridging mechanisms in the cementitious composites as a result of the high specific surface area of SNS and the strong chemical and physical bonding of SNS with the hydration phases. The SNS materials offers strong advantages over graphene-based materials on improving the engineering properties of cementitious materials and reducing their cost and CO_2 emissions.

Highlights

* Corresponding author. E-mail address: yin.chi@whu.edu.cn (Yin Chi). m.saafi@lancaster.ac.uk (Mohamed Saafi)

- Treated and non-treated SNS flakes enhanced the mechanical and fracture properties of the cementitious composites.
- The SNS strengthening and toughening mechanisms in the cementitious composites are crack bridging and crack deflection.
- The SNS induced performance enhancement similar to that of graphene-based materials.

Key Words

Bio-nanoplatelets; Cementitious composites; Mechanical properties; Fracture properties

1. Introduction

Ordinary Portland Cement (OPC), the key ingredient of concrete, is responsible for 8-9% of the global CO_2 emissions [1]. Because there are no other cementitious materials that can replace OPC in the foreseeable future to meet the need for future physical infrastructure, its global demand is forecasted to increase by about 50% by 2050 [2,3], resulting in significant increase in CO_2 emissions. One of the popular approaches to reduce the consumption of OPC-based materials involves the use of the so-called "do more with less" method where different types of additives are added to cementitious materials to improve their engineering properties. As a result, smaller size structural members can be designed which in return reduces both the volume of concrete and the demand for OPC.

Various types of macro fibers have been employed to improve the engineering properties of cementitious composites. For example, high-strength steel, polypropylene polyvinyl alcohol (PVA), polyethylene glycol (PEG) and carbon fibers were commonly used to enhance the mechanical and fracture properties of cementitious composites [4–9].

Micro and nanofibers were found to outperform macrofibers for improving the microstructure and overall mechanical properties of cementitious composites. Owing to their chemical functional groups and small size, carbonaceous materials such as carbon nanotubes

(CNTs), graphene and graphene oxide (GO) promote the hydration of the cement particles which in return increases the amount of the calcium silicate hydrate (C-S-H) phases [10–15]. These materials also strengthen the hydration phases. Unlike CNTs, the high specific surface area of graphene and GO materials creates stronger and more crack resistant cementitious composites [16,17].

The large-scale application of CNTs, graphene and GO in cementitious materials however is limited. This is because these carbonaceous materials are expensive, their production is energy intensive and pose serious health and safety issues [18]. In addition, they are incompatible with cementitious materials as they tend to agglomerate in water thus degrading their mechanical properties [19]. Bio-based materials are considered as a low-cost and sustainable alternative to micro and nanofibers. Previous research has shown that cellulose nanofibers (CNFs) and cellulose nanocrystals (CNCs) [20,21] chemically interact with cement, thereby improving its hydration kinetics. Because of this, CNFs and CNCs help improve the formation and growth of the hydration phases [22]. However, CNFs and CNCs have moderate effect on the mechanical and fracture properties of cementitious composites due to their small specific surface area [23].

Therefore, there is a genuine need for new low cost and environmentally friendly materials as alternatives to graphene, GO, CNT, CNF and CNC reinforcing materials. Recently, we successfully synthesized 2D SNS flakes for applications in cementitious composites. Compared with graphene-based materials, SNS has higher specific surface area and richer in chemical hydroxyl functional groups which enables the SNS flakes to chemically interact with both the cement particles during hydration and the produced hydration phases [24,25]. The SNS material is also significantly cheaper than graphene-based materials and its production is scalable for large deployment in the construction industry. Our Density Functional Theory (DFT) and Molecular Dynamics (MD) simulations and Electrochemical (EC) characterization have shown that the SNS flakes significantly improve the hydration kinetics of cement and increases the mechanical properties of C-S-H globules [26,27]. However, the strengthening and toughening mechanisms in SNS doped cementitious composites are not yet fully understood and the resulting macro engineering properties are still unknown. As such, this paper aims to elucidate the role of the SNS flakes in improving the mechanical and fracture properties of cementitious. An extensive experimental program was carried out to determine the influence of SNS on the compressive, tensile, and flexural strength, flexural modulus, fracture energy and fracture toughness of the cementitious composites. The experimental parameters considered in this program were SNS concentration (0, 0.1, 0.2, 0.3-wt%), SNS treatment (sonicated and non-sonicated) and w/c ratio (0.35 and 0.40).

2. Experimental program

2.1 Materials

Ordinary Portland Cement (OPC), CEM I 52.5R (Hanson, UK) was used to prepare the cement pastes. Table 1 and Table 2 list the OPC physical properties and chemical composition. The main components of OPC are CaO (64.98%), SiO_2 (20.85%) and Al_2O_3 (5.22%) with a particle size ranging from 5 to 30 μm and a relative density of 2.75-3.20. These properties meet the requirements of B.S EN 197-1:2011 standard [28]. A Polycarboxylic ether-based superplasticizer (SP) (MasterGlenium®51, BASF, UK) was used at a concentration of 1-wt% to improve the workability of the cement pastes. The SNS flakes were synthesized by our industrial partner, Cellucomp Limited (UK). The SNS flakes are 50 μm in width, 50 μm in length and 0.25 μm in thickness. And their specific surface area and density are 68.35 m^2/g and 1.31g/cm^3, respectively.

The manufacturing process for the SNS flakes is described in [26,27]. The first step in this process involved diluting the sugar beet pulp with a solid content of 1% by weight.

Subsequently, the pH of the solution was increased to 14 using 0.5 M sodium hydroxide (NaOH). The NaOH was purchased from Honeywell Fluka™ and a purity of 98%. This enables the removable of the hemicellulose and pectin from the mixture. The mixture was then thermally treated at 90 ℃ for 5 hours and periodically homogenized for 1 hour with a stirring blade rotating at 700 rpm. At the end of the thermal treatment, the mixture was homogenized for 5 minutes at 1900 rpm. The SNS mixture was then filtered and a SNS paste with a solid content of 4 to 8-wt%was obtained.

2.2 Mix proportions and specimen preparation

The mix proportions adopted in this study were divided into two groups (groups A and B) as shown in Table 3. In all groups, the cement pastes were doped with SNS at concentrations of 0.0, 0.1, 0.2 and 0.3-wt%. In group A, cement pastes with a w/c ratio of 0.35 were doped with as-received SNS (samples AR) and treated SNS (samples AT). In group B, the cement pastes with a w/c ratio of 0.4 were doped with as-received SNS (samples BR) and treated SNS (samples BT). The samples AP in group A and BP in group B were used as plain samples for reference purposes. The treatment of SNS consisted of sonicating the SNS solution for 30 minutes. In this treatment process, the required amount of SNS was first added to the required amount of water and SP. Subsequently, the solution was sonicated in an ice bath with a sonifier (Branson Sonifier 450) at 50% duty cycles. The as-received SNS solution was prepared by manually stirring the mixture of the required amount of SNS, water and SP.

The cement pastes were prepared according to ASTM C305-20 [29]. The cement powder and the SNS solution were first mixed for 30 seconds at a mixing speed of 140 revolutions/min, then mixed for 120 seconds at a mixing speed of 285 revolutions/min until the SNS flakes were evenly dispersed in the fresh cement paste. The cement pastes were poured into 40 mm x 40 mm x 160 mm and 50 mm x 50 mm x 50 mm steel molds. The molds were placed on a vibrating table and vibrated for 60 seconds. The molds were covered with a plastic film to prevent water evaporation and left to cure at room temperature for 24 hours. The samples were then demolded and placed in a standard curing tank with water temperature of 20±2℃ until testing.

2.3 Workability and mechanical properties

A mini-slump test was conducted to determine the influence of the SNS flakes on the workability of the cement pastes. This was done by measuring the spread diameters formed by the pastes upon lifting the mini-slump cone [30,31]. The top and bottom diameters and the height of the cone are 70 mm, 100 mm and 60 mm, respectively. The workability of the cement pastess was measured according to [32]. The workability W of the cement pastes was determined using the following equation [33]:

$$\mathrm{W} = \left(\frac{\frac{(d_1 + d_2)}{2} - d_0}{d_0}\right) \times 100 \tag{1}$$

where d_1 and d_2 are the two direction spread-out diameters of the paste and d_0 is the bottom diameter of the cone.

The mechanical properties were determined at 28 days of curing. The compressive strength of the cementitious composites was determined according to ASTM C 109 standard [34]. A total of 56 cubes (50 mm in side) were tested using a universal testing machine (UTM, 250 kN) at a loading rate 0.5 MPa/s. The splitting tensile strength of the cementitious composites was evaluated according to BS EN12390-6:0229 [35] using UTM. A total of 42 cylinders (100 mm x 200 mm) were tested with a loading rate of 0.06 MPa/s. A total of 56 prisms (40 mm x 40 mm x 160 mm) were subjected to four-point bending test according to ASTM C78 [36] using UTM at loading rate of 0.5 MPa/s to determine the flexural strength and flexural modulus of the cementitious composites.

2.4 Fracture properties

The fracture properties of the cementitious composites were evaluated using the three-point bending test method according to the RILEM standard (1985). A total of 56 notched prisms (40 mm ×40 mm × 160 mm) were tested using UTM at a displacement rate of 0.02 mm/min. The notch depth and height are 3 mm and 16 mm, respectively. As shown in Fig.1, during loading, the crack mouth opening displacement (CMOD) was measured with a video gauge^{TM} (Imetrum Ltd). The video gauge consisted of two camera lenses, an Imetrum controller and a computer data acquisition system. Uniform black dots were printed on the surface of the prism around the notch. The printed area defines the region where the displacement is measured. To capture the positions of the dots during testing, the lenses were placed 1.2 m from the prism surface. The load, prism deflection and positions of the dots were recorded at a frequency 15 Hz. The CMOD was obtained by monitoring the horizontal displacement between the two dots adjacent to the mouth of the crack. This was achieved by collecting measurements generated by the video gauge in the form of pixel displacement. During testing, a series of pixel displacement results was recorded and the pixel displacement was then converted to real displacement in mm by the data acquisition system software.

The measured applied load (P), deflection (δ) and CMOD were used to calculate the fracture energy (G_F) and fracture toughness (K_{IC}) using the following equations [38].

$$G_F = \frac{mg\delta_0 + W_0}{t(h-a)} = \frac{mg\delta_0 + \delta_0^{\delta_0} P(\delta)d\delta}{t(h-a)} \quad (2)$$

$$K_{IC} = \frac{P_{max}S}{th^{\frac{3}{2}}} f\left(\frac{a}{h}\right) \quad (3)$$

$$f\left(\frac{a}{h}\right) = 2.9\left(\frac{a}{h}\right)^{\frac{1}{2}} - 4.6\left(\frac{a}{h}\right)^{\frac{3}{2}} + 21.8\left(\frac{a}{h}\right)^{\frac{5}{2}} - 37.6\left(\frac{a}{h}\right)^{\frac{7}{2}} + 38.7\left(\frac{a}{h}\right)^{\frac{9}{2}} \quad (4)$$

where G_F is the fracture energy, m is the mass ($m = m_1 + m_2$), m_1 is the mass of the prism between supports, m_2 is the mass of the loading fixture, g is the gravity acceleration, δ_0 is the final displacement of the failure prism, W_0 is the area under the load-displacement curve, t is the thickness of the prism, h is the height of the prism, a is the depth of the notch, K_{IC} is the fracture toughness, P_{max} is the peak load and S is the span of the prism.

2.5 Characterization of SNS and cementitious composites

The SNS flakes were characterized to determine their functional groups, crystal structure and morphology. The as-received SNS material was dried, and samples were prepared for characterization. Fourier-transform infrared (FTIR) spectrometer (Agilent Technologies ExoScan 4100) was employed to determine the chemical properties of the SNS flakes. The SNS sample was subjected to 128 consecutive scans in the frequency range of 4000-500 cm^{-1} at a spectral resolution of 8 cm^{-1}. The obtained infrared absorption spectrum was used to identify the functional groups of SNS. Single-crystal X-ray diffractometer (XRD) (Agilent SuperNova) was used to analyze the crystal structure of the SNS flakes. The XRD patterns of SNS were recorded in the range of 5° to 65° (2θ) with a scanning rate of 2°/min, with a step size of 0.01°.

Analytical field emission scanning electron microscope (FE-SEM) with an energy dispersive X-ray spectroscopy (EDS/EDX) system (JEOL JSM-7800F) was employed to observe the morphology of the SNS flakes. The EDS/EDX system has a Silicon Drift Detector (SDD) (X-Max50) of an area of 50 mm^2. The SNS sample was coated with gold prior to the characterization then transferred to the instrument vacuum chamber and characterized at an accelerating voltage of 2-15 kV at ambient temperature.

The morphology of the SNS flakes was further evaluated using transmission electron microscope (TEM) (JEM-1010). To generate TEM images of the sample, a SNS solution with a concentration of 0.2-wt% was prepared. The SNS suspension was then dripped onto carbon-coated TEM grids and allowed to air-dry at room temperature. The TEM imaging was then performed at an acceleration voltage of 80 kV.

The microstructure of the cementitious composites was characterized at 28 days. Samples recovered from broken prisms were ground into powder by a planetary ball-mill (grinding machine PM 100) and used to identify the crystal structure of the cementitious composites using XRD. Samples recovered from broken prisms were also polished into small pellets then coated with gold to determine the morphological features of the cementitious composites using SEM/EDX.

3. Experimental results and discussion

3.1 Characterization of SNS

Fig. 2 shows a typical SEM image of the SNS flakes along with their elemental mapping analysis and chemical composition. As shown, the SNS flakes are mainly composed of carbon (54.4%) and oxygen (43.1%). Impurities such as calcium (1.3%), chlorine (0.6%), sodium (0.4%) and aluminum (0.2%) from the preparation process are also shown in Fig. 2. The FTIR spectrum of the SNS flakes is shown in Fig. 3a. The absorbance peak of around 3350 cm^{-1} represents the stretching vibration of the hydroxy group (O-H), which indicates the hydrophilicity of the SNS flakes [39,40]. The prominent peak at 2850 cm^{-1} is due to the stretching and vibration of saturated C-H in cellulose [41]. The peak at 1675 cm^{-1} reflects the stretched O-H groups, which corresponds to the adsorbed water molecules. The 1470, 1420, 1360 and 970 cm^{-1} bands are attributed to C-H stretching of methylene (CH_2) and methyl (CH_3) groups. The signal at 1170 cm^{-1} indicates a C-O-C bond, which is the characteristic of cellulose ethers [42–44]. The functional groups of the SNS flakes provide unique advantages over carbonaceous materials as they allow the SNS flakes to disperse in water and chemically interact with the cement particles and hydration phases, thereby improving the hydration and engineering properties of the cementitious composites.

The XRD pattern of SNS is shown in Fig. 3b. As depicted in this figure, the SNS exhibits diffraction peaks around 2θ=16.5° and 22.5°. This indicates that SNS has typical cellulose-I structural features. The peak at 2θ =16.5° represents the SNS crystalline (110) plane. In this plane, the surfaces of the SNS flakes are decorated with mainly hydroxyl groups with some hydrophilic groups. The hydroxyl groups promote the dispersion of the SNS flakes in water [45]. The diffraction peak at 2θ =22.5° was attributed to the (200) plane where the SNS consists of lignin and hemicellulose [45,46].

The crystallinity index (CI) value obtained from XRD is an indication of how mechanically strong the SNS flakes are. The CI value of the SNS flakes can calculated using the following equation [47]:

$$CI = 100 \times \frac{I_{200} - I_{AM}}{I_{200}} \tag{5}$$

Where I_{200} represents the maximum intensity of the (200) diffraction peak, located around 2θ=22.5°, I_{AM} is the minimum diffraction intensity of the amorphous SNS (2θ=18°) between the 2θ=16.5° and 22.5° [48]. Based on equation (5), the average *CI* value for the SNS flakes is 75.65%. This relatively high *CI* value suggests that the SNS flakes possess high stiffness, rigidity and strength [49].

Fig. 3c-d depict SEM images of the SNS flakes. These images indicate the sample is composed of stacked and overlapped SNS sheets. The SNS sheets display wrinkled, crumpled and rippled features. Graphene based 2D materials also possess these features. The TEM images of the SNS flakes are shown in Fig. 3e-f. The purity of the SNS product is high, which clearly shows that most of the hemicellulose and lignin have been removed during the fabrication process. As can be seen, the SNS flakes are composed of intertwined and randomly oriented cellulose nanofibers with a diameter of about 40 nm.

3.2 *Workability, compressive and tensile strength of SNS cement pastes*

Fig. 4a shows the influence of SNS on the workability of the cement pastes. The workability *W* of the plain cement paste is 136%. As shown, the addition of 0.1 and 0.2-wt% SNS did not affect the workability of the cement pastes significantly. However, the addition of 0.3-wt% SNS reduced the workability of the cement paste by 33.4%.

Fig. 4b-c plot the compressive strengths of the cementitious composites as a function of SNS concentration for w/c ratios for 0.35 and 0.40 at 28 days of curing. These figures also compare the effect of the as-received and treated SNS flakes on the compressive strength of the cementitious composites. All cementitious composites reached their maximum compressive strength at a concentration of 0.2-wt%. The cementitious composites doped with the treated SNS flakes showed slightly higher compressive strength than those with the as-received SNS flakes. In addition, the cementitious composites with the w/c ratio of 0.35 showed higher compressive strength than those with the w/c ratio of 0.40. However, as shown in Fig. 4d, the cementitious composites with the w/c ratio of 0.4 exhibit slighter better percentage increase in the maximum compressive strength. At the w/c ratio of 0.35, the treated and as-received SNS flakes increased the compressive strength by as much as 11.51% and 8.35%, respectively, whereas at the w/c ratio of 0.4, the treated and as-received SNS flakes increased the compressive strength by as much as 13.24% and 9.94%, respectively. However, for all cementitious composites the improvement of the compressive strength diminished at 0.3-wt% SNS.

Fig. 5a-b show the effect of SNS on the splitting tensile strength of the cementitious composites at 28 days. The change in the tensile strength as a function of SNS concentration trend is similar to that of the compressive strength. For all cementitious composites, the addition of 0.2-wt% SNS yielded the highest tensile strength. This improvement is more noticeable for cementitious composites with the w/c ratio of 0.35 where the treated and as-received 0.2-wt% SNS enhanced the tensile strength by 37.6% and 33.3%, respectively (Fig. 5c). At the w/c ratio of 0.4, the 0.2-wt% treated and as-received SNS flakes improved the tensile strength by 32.8% and 31.2%, respectively (Fig. 5c). The enhancement of the tensile strength degraded at 0.3-wt% SNS.

3.3 Flexural properties

As depicted in Fig. 6a-b, the treated and as-received SNS flakes have somewhat different effects on the flexural strength. The flexural strength of the cementitious composites doped with the as-received SNS increased with SNS dosage, reaching its maximum at 0.2-wt%, then decreased at 0.3-wt%. On the other hand, the flexural strength of the cementitious composites doped with treated SNS is somewhat plateaued between 0.1-wt% and 0.2-wt% then decreased at 0.3-wt%. The treated SNS flakes seemed to outperform the as-received SNS flakes, presumably due to better dispersion. The cementitious composites with the w/c ratio of 0.35 exhibited a maximum flexural strength percentage increase of about 37.5% and 31.7% for treated and as-received SNS, respectively (Fig. 6c). When the w/c ratio is increased to 0.4, the treated and as-received SNS flakes improved the flexural strength by as much as 39.5% and 28.4%, respectively (Fig. 6c).

Fig. 7 shows the load-deflection responses of the cementitious composites. Overall, the addition of SNS improved the flexural behavior of the cementitious composites. The failure load, and flexural toughness and flexural modulus were all improved. The treated SNS flakes improved the flexural behavior of the cementitious composites with the w/c ratio of 0.35 more than the other cementitious composites. One noticeable enhancement is in the flexural modulus as shown in Fig. 8, Figs. 8a-b indicate that the flexural modulus increased with increasing SNS dosage. At the w/c ratio of 0.35, the cementitious composites with treated and as-received SNS flakes reached the same maximum flexural modulus at 0.2-wt%, yielding a percentage increase of about 32.69% (Fig. 8c). This percentage increase decreased at 0.3-wt% SNS (Fig. 8a). The flexural modulus of the cementitious composites containing treated SNS flakes with the w/c ratio of 0.4 increased at 0.1-wt% and remained constant at 0.2-wt%, then slightly decreased at 0.3-wt% (Fig. 8b). In this case, the treated SNS flakes increased the flexural modulus by as much as 30.6% (Fig. 8c). At the w/c ratio of 0.4, the as-received SNS flakes also improved the flexural modulus of the cementitious composites. A dosage of 0.2-wt% as-received SNS produced the same maximum flexural modulus as the treated 0.1-wt% and 0.2-wt% SNS (i.e., maximum percentage increase of 30.6%). However, the improvement of the flexural modulus significantly diminished at 0.3-wt% (Fig. 8b).

3.4 Fracture properties

The load-deflection responses of the notched prisms obtained from the three-point deflection tests are depicted in Fig. 9. The addition of treated and as-received SNS flakes enhanced the peak load and flexural modulus of the cementitious composites. The SNS flakes also increased the areas under the load-deflection curves and the maximum deflections (Fig. 9). In Fig. 10a-b, the fracture energy (G_F) of the cementitious composites is plotted against SNS concentration. As can be seen, the cementitious composites with the w/c ratio of 0.35 outperformed the cementitious composites with the w/c ratio of 0.4. At the w/c ratio of 0.35, G_F increased with increasing treated SNS dosage up to 0.2-wt% then dropped slightly at 0.3-wt%. Similarly, at this w/c ratio of 0.35, G_F increased with increasing as-received SNS dosage, followed by a significant drop at 0.3-wt%. As shown in Fig. 10c, at the w/c ratio of 0.35, the maximum percentage increase in G_F is 67.8% and 54.5% for treated and as-received SNS reinforced cementitious composites, respectively.

At the w/c ratio of 0.4, the addition of as-received SNS flakes increased G_F linearly up to 0.2-wt% then diminished at 0.3-wt% (Fig. 10c). The treated SNS flakes however increased G_F at 0.1-wt% after which their effect slowed and reached its maximum at 0.2-wt%. This enhancement also diminished at 0.3-wt%. The observed maximum percentage increase in G_F is 66.6% and 40.3% for treated and as-received SNS reinforced cementitious composites, respectively (Fig. 10c).

From Fig. 11, we can see that the enhancement of the fracture toughness (K_{IC}) somewhat follows the enhancement trend of G_F. All SNS reinforced cementitious composites reached their maximum K_{IC} at 0.2-wt% where for the cementitious composites with the w/c ratio of 0.35, the treated and as-received SNS flakes increased K_{IC} by 49.6% and 42.4%, respectively (Fig. 11c). At the w/c ratio of 0.4, the treated and as-received SNS flakes increased K_{IC} by 43.7% and 19.6%, respectively (Fig. 11c).

The enhancement of G_F and K_{IC} is reflected in the load-CMOD curves depicted in Fig. 12. As can be seen, all load-curves have similar shapes. The pre-peak slopes of the load-CMOD curves are similar. However, the SNS flakes increased the peak load in the load-CMOD curves of the cementitious composites, but they do not seem to affect the CMOD values at the peak loads. The post-cracking behavior of the cementitious composites with the w/c ratios of 0.35 is different from that of the cementitious composites with the w/c ratio of 0.4. At the w/c ratio of 0.35, the load decreased gradually while at the w/c ratio of 0.4, the load decreased somewhat rapidly (Fig. 12). This means, the area under the load-CMOD curves for the cementitious composites with the w/c of 0.35 is larger than that for the cementitious composites with the w/c ratio of 0.4, thus better post-cracking behavior. As depicted in Fig. 12a-b, the treated SNS flakes outperformed the as-received SNS flakes in enhancing the post-cracking behavior of the cementitious composites with the w/c ratio of 0.35. However, they slightly improved the post-cracking behavior of the cementitious composites with the w/c ratio of 0.4 (Fig. 12c-d).

3.5 Microstructure characterization

Fig. 13 illustrates XRD patterns and analysis of the cementitious composites containing 0 and 0.3-wt% SNS at the w/c ratio of 0.35 at 28 days. As can be seen from Fig. 13, the XRD pattern analysis revealed that the microstructure of the cementitious composites consists of alite (C_3S, COD 96-901-5085), ettringite (COD 96-901-5085), $Ca(OH)_2$ (COD 96-100-8782), calcite ($CaCO_3$, COD 96-900-9669) and carbonated calcium hemicarboaluminate (COD 96-210-5252).. The addition of SNS does not change the microstructure of the cementitious composites in term of hydration phases but it does alter the crystal diffraction peak intensities. The results of the Rietveld refinements shown in Fig. 13, demonstrate that the quantity of ettringite and $CaCO_3$ have increased from 8.4% and 21.3% to 15.6% and 31.4%, respectively. The amount of $Ca(OH)_2$ has decreased from 49.2% to 47.2%, while the content of alite and carbonated calcium hemicarboaluminate has decreased to 3.6% and 2.1%. It is well known that the intensity peaks corresponding to C-S-H phases are not detectable in the XRD patterns. However, the change in the C-S-H phases can be quantified by evaluating the change in the peak intensity of the other hydration phases such as $Ca(OH)_2$. As can be seen, the intensity peaks corresponding to ettringite and $CaCO_3$ increased with SNS dosage of 0.3-wt%. This means, the SNS flakes are effective in increasing C-S-H and other hydration phases especially for the cementitious composites infused with SNS.

Fig. 14 illustrates typical SEM images of the cementitious composites doped with treated SNS flakes at concentrations of 0.0, 0.1, 0.2 and 0.3-wt% at the w/c ratio of 0.35 at 28 days of curing. As depicted in Fig. 14a, the microstructure of the plain cement matrix is mainly composed of unhydrated cement particles, a small amount of calcium hydroxide (CH) and C-S-H. The microstructure also contains wide cracks (Fig. 14a), which can be attributed to the shrinkage. The addition of 0.1-wt% of treated SNS flakes increased the amount of the CH and C-S-H hydration phases and reduced crack propagation and crack width significantly (Fig. 14b-d). The addition of 0.2-wt% of treated SNS flakes further increased the amount of CH particles (Fig. 14c). These CH particles are in the form of hexagonal crystals that are uniformly distributed throughout the matrix. These CH crystals appear to be intercalated with the SNS flakes, thereby reducing shrinkage which resulted in a microstructure with fewer cracks and pores. We can also see from Fig. 14d that the inclusion of 0.3-wt% of treated SNS reduced the size of the CH crystals and produced CH/SNS agglomerates.

3.6 Discussion

The experimental results show that the SNS flakes are effective in improving the mechanical and fracture properties of the cementitious composites. Compared with graphene-based flakes, the SNS flakes are richer in hydroxyl functional groups thus they show good dispersibility in water. The workability of the cementitious pastes was not affected by the addition of the SNS flakes at 0.1 and 0.2-wt% dosages. However, the workability results suggest that higher SNS dosages reduce the workability of the cementitious composites. This could be attributed to the high specific surface area and high hydrophilicity of the SNS flakes. When used in high concentrations, SNS tends to absorb free water, thereby, increasing the internal friction between the cement particles which in turn reduces the workability of the cement pastes [24]. This trend was also observed in GO doped composites [50]. The SNS flakes improved the formation of the hydration phases of cement due to their high number of reactive functional groups. Because of this, the hydration kinetics in cementitious composites with SNS are superior to those in cementitious composites with graphene-based materials [27]. It appears that the addition of SNS altered the morphology of the cementitious composites. The SNS flakes regulated the microstructure by reducing cracks and creating denser microstructure with intercalated hexagonal CH/SNS particles.

Like graphene-based flakes, the SNS flakes improved the compressive strength of the composites. However, this improvement is moderate due to the restrictive properties of the cementitious materials when they are subjected to compressive stress. The observed maximum compression strength enhancement percentages are within the range of the percentages obtained from cementitious composites doped with graphene-based flakes. This means SNS and graphene-based materials have similar effects on the compressive strength of cementitious composites. The other mechanical properties such as splitting tensile and flexural strength, flexural modulus and fracture properties were also improved.

The tensile and flexure strength, flexural modulus and fracture properties of the cementitious composites were enhanced due to the inherent properties of the SNS flakes. These flakes have high specific surface area that contains many functional groups. These properties along with the SNS geometric features such as wrinkles and ripple enable the SNS flakes to form strong chemical and mechanical bonds with the hydration phases. This enhances the toughening and strengthening mechanisms induced by the SNS flakes in the cementitious composites. The strong interfacial bond between the SNS flakes and the hydration phases prevents the pull-out of the SNS flakes thereby linking them together to form a denser and packed microstructure with fewer cracks. Another important toughening mechanism induced by the SNS flakes is crack deflection. In this mechanism, cracks are deflected when the SNS flakes are present in their crack propagation paths. In this case, cracks find it hard to further propagate along their initial paths. As a result, they are delayed and then get deflected to regions without SNS flakes. This enables the cracks to take tortuous paths, thereby improves the flexural strength, flexural modulus, and fracture energy and fracture toughness of the cementitious composites as depicted in Fig. 6, Fig. 8, Fig. 10 and Fig. 11. The failure modes of the prisms subjected to four-point bending are given in Fig. 15. As can be seen, the plain prism (0-wt% SNS) failed in tension where the crack propagated straight from the bottom of the prism. However, for the cement prisms doped with the SNS flakes, zig-zag type-cracks were formed in the bottom side of the prisms due to the crack deflection mechanism, then propagated along their depths. As can be seen in Fig. 15, these tortuous crack propagation paths were formed with somewhat kick angles.

As expected, increasing the w/c ratio from 0.35 to 0.4 resulted in lower mechanical and fracture properties. The treated SNS flakes outperformed the as-received SNS flakes in improving the mechanical and fracture properties of the cementitious composites. However, the as-received SNS flakes produced acceptable percentage increases in these properties. This makes SNS flakes attractive for large-scale applications as they can be used in cementitious materials without treatment.

Even though the inherent mechanical properties of SNS are much lower than those of graphene-based materials, the obtained percentage increases in the compressive, tensile and flexural strength and fracture properties (including fracture properties) are within the range of the percentage increases obtained from cementitious composites doped with graphene-based materials [51]. This is significant because the cost and carbon footprint of SNS are much lower than those of graphene-based materials, thus making it a serious alternative reinforcing material in cementitious composites.

4. Conclusions

In this paper, we demonstrated that inexpensive and environmentally friendly biobased SNS flakes can improve the mechanical and fracture properties of cementitious materials. An extensive experimental program was carried to examine the performance of cementitious composites doped with treated and as-received SNS flakes using two w/c ratios. Based on the experimental results, the following main conclusions can be drawn:

- Owing to their high specific area and large number of reactive functional groups, the SNS flakes improved the hydration kinetics of the cementitious materials. These inherent properties along with their geometric features such as wrinkles and ripples seemed to improve the chemical and mechanical bonds between the SNS flakes and the hydration phases. This improved the engineering properties of the cementitious composites.
- The SNS flakes slightly improved the compressive strength of the cementitious composites, but they were more effective in increasing the tensile and flexural strength, flexural modulus, fracture energy and fracture toughness of the cementitious composites. This was due to the toughening mechanisms produced by SNS, mainly crack bridging and crack deflection.
- The SNS flakes produced percentage increases in mechanical and fracture properties similar to those produced by other competitor materials such as graphene and GO. This means SNS can be used as replacement for enhancing the performance of construction materials.
- Both treated and non-treated SNS present a new cost-effective and sustainable way for creating greener, stronger and durable construction materials that could have the potential of reducing the consumption and carbon footprint of OPC in the construction industry.

Acknowledgement

This research work is financially supported by the European Commission Horizon 2020 Marie Sklodowska-Curie Research Grant (B- SMART 799658) and the Scientific Research Foundation of Hunan provincial Education Department of China (22B0473). The authors are also grateful for the support from the National Natural Science Foundation of China (51878519).

Reference

[1] P.J.M. Monteiro, S.A. Miller, A. Horvath, Towards sustainable concrete, Nat. Mater. 16 (2017) 698–699.

[2] S.A. Miller, G. Habert, R.J. Myers, J.T. Harvey, Achieving net zero greenhouse gas emissions in the cement industry via value chain mitigation strategies, One Earth. 4 (2021) 1398–1411. https://doi.org/10.1016/j.oneear.2021.09.011.

[3] C. Zhou, J. Wang, X. Shao, L. Li, J. Sun, X. Wang, The feasibility of using ultra-high performance concrete (UHPC) to strengthen RC beams in torsion, J. Mater. Res. Technol. 24 (2023) 9961–9983. https://doi.org/10.1016/j.jmrt.2023.05.185.

[4] M. Hsie, C. Tu, P.S. Song, Mechanical properties of polypropylene hybrid fiber-reinforced concrete, Mater. Sci. Eng. A. 494 (2008) 153–157.

[5] P.S. Song, S. Hwang, Mechanical properties of high-strength steel fiber-reinforced concrete, Constr. Build. Mater. 18 (2004) 669–673.

[6] S. Wang, V.C. Li, Polyvinyl alcohol fiber reinforced engineered cementitious composites: material design and performances, in: Proc., Int'l Work. HPFRCC Struct. Appl. Hawaii, Citeseer, 2005.

[7] Y. Zhou, C.A. Orozco, E. Duque-Redondo, H. Manzano, G. Geng, P. Feng, P.J.M. Monteiro, C. Miao, Modification of poly (ethylene glycol) on the microstructure and mechanical properties of calcium silicate hydrates, Cem. Concr. Res. 115 (2019) 20–30.

[8] Z. Xiong, W. Wei, S. He, F. Liu, H. Luo, L. Li, Dynamic bond behaviour of fibre-wrapped basalt fibre-reinforced polymer bars embedded in sea sand and recycled aggregate concrete under high-strain rate pull-out tests, Constr. Build. Mater. 276 (2021) 122195. https://doi.org/10.1016/j.conbuildmat.2020.122195.

[9] C. Zhou, J. Wang, W. Jia, Z. Fang, Torsional behavior of ultra-high performance concrete (UHPC) rectangular beams without steel reinforcement: Experimental investigation and theoretical analysis, Compos. Struct. 299 (2022) 116022. https://doi.org/10.1016/j.compstruct.2022.116022.

[10] M.S.M. Norhasri, M.S. Hamidah, A.M. Fadzil, Applications of using nano material in concrete: A review, Constr. Build. Mater. 133 (2017) 91–97.

[11] M.S. Konsta-Gdoutos, Z.S. Metaxa, S.P. Shah, Highly dispersed carbon nanotube reinforced cement based materials, Cem. Concr. Res. 40 (2010) 1052–1059.

[12] M.M. Mokhtar, S.A. Abo-El-Enein, M.Y. Hassaan, M.S. Morsy, M.H. Khalil, Mechanical performance, pore structure and micro-structural characteristics of graphene oxide nano platelets reinforced cement, Constr. Build. Mater. 138 (2017) 333–339. https://doi.org/10.1016/j.conbuildmat.2017.02.021.

[13] S. Chuah, Z. Pan, J.G. Sanjayan, C.M. Wang, W.H. Duan, Nano reinforced cement and concrete composites and new perspective from graphene oxide, Constr. Build. Mater. 73 (2014) 113–124.

[14] B. Huang, J. Wang, G. Piukovics, N. Zabihi, J. Ye, M. Saafi, J. Ye, Hybrid cement composite-based sensor for in-situ chloride monitoring in concrete structures, Sensors Actuators B Chem. 385 (2023) 133638. https://doi.org/10.1016/j.snb.2023.133638.

[15] J. Sun, S. Lin, G. Zhang, Y. Sun, J. Zhang, C. Chen, A.M. Morsy, X. Wang, The effect of graphite and slag on electrical and mechanical properties of electrically conductive cementitious composites, Constr. Build. Mater. 281 (2021) 122606. https://doi.org/10.1016/j.conbuildmat.2021.122606.

[16] M. Murali, W.S. Alaloul, B.S. Mohammed, M.A. Musarat, M. Al Salaheen, A.M. Al-Sabaeei, A. Isyaka, Utilizing graphene oxide in cementitious composites: A systematic review, Case Stud. Constr. Mater. 17 (2022) e01359. https://doi.org/10.1016/j.cscm.2022.e01359.

[17] Y. Tang, Z. Huang, Z. Chen, M. Chen, H. Zhou, H. Zhang, J. Sun, Novel visual crack width measurement based on backbone double-scale features for improved detection automation, Eng. Struct. 274 (2023) 115158. https://doi.org/10.1016/j.engstruct.2022.115158.

[18] M.S. Soffian, F.Z. Abdul Halim, F. Aziz, M. A．Rahman, M.A. Mohamed Amin, D.N. Awang Chee, Carbon-based material derived from biomass waste for wastewater treatment, Environ. Adv. 9 (2022) 100259. https://doi.org/10.1016/j.envadv.2022.100259.

[19] Y. Gao, H. Jing, Z. Zhou, W. Chen, M. Du, Y. Du, Reinforced impermeability of cementitious composites using graphene oxide-carbon nanotube hybrid under different water-to-cement ratios, Constr. Build. Mater. 222 (2019) 610–621. https://doi.org/10.1016/j.conbuildmat.2019.06.186.

[20] R.K. Abu Al-Rub, B.M. Tyson, A. Yazdanbakhsh, Z. Grasley, Mechanical properties of nanocomposite cement incorporating surface-treated and untreated carbon nanotubes and carbon nanofibers, J. Nanomechanics Micromechanics. 2 (2012) 1–6.

[21] Y. Cao, P. Zavaterri, J. Youngblood, R. Moon, J. Weiss, The influence of cellulose nanocrystal additions on the performance of cement paste, Cem. Concr. Compos. 56 (2015) 73–83. https://doi.org/10.1016/j.cemconcomp.2014.11.008.

[22] M.Y. Xuan, X.Y. Wang, Multi-technique investigation regarding the impact of cellulose nanofibers on ultra-high-performance concrete at the macroscopic and microscopic levels, Constr. Build. Mater. 327 (2022) 126936. https://doi.org/10.1016/j.conbuildmat.2022.126936.

[23] S. Nassiri, Z. Chen, G. Jian, T. Zhong, M.M. Haider, H. Li, C. Fernandez, M. Sinclair, T. Varga, L.S. Fifield, M. Wolcott, Comparison of unique effects of two contrasting types of cellulose nanomaterials on setting time, rheology, and compressive strength of cement paste, Cem. Concr. Compos. 123 (2021) 104201. https://doi.org/10.1016/j.cemconcomp.2021.104201.

[24] H. Hasan, B. Huang, M. Saafi, J. Sun, Y. Chi, E. Whale, D. Hepworth, J. Ye, Novel engineered high performance sugar beetroot 2D nanoplatelet-cementitious composites, Constr. Build. Mater. 202 (2019) 546–562. https://doi.org/10.1016/j.conbuildmat.2019.01.019.

[25] B. Huang, Y. Chi, T. Almotlaq, J. Wang, M. Saafi, J. Ye, J. Sun, Y. Wang, J. Ye,

Influence of sugar beetroot microsheets on the hydration kinetics of cementitious composites : Electrochemical characterization, Cem. Concr. Compos. 144 (2023) 105314. https://doi.org/10.1016/j.cemconcomp.2023.105314.

[26] Y. Chi, B. Huang, M. Saafi, J. Ye, C. Lambert, Carrot-based covalently bonded saccharides as a new 2D material for healing defective calcium-silicate-hydrate in cement: Integrating atomistic computational simulation with experimental studies, Compos. Part B Eng. 199 (2020) 108235.

[27] Y. Chi, B. Huang, M. Saafi, N. Fullwood, C. Lambert, E. Whale, D. Hepworth, J. Ye, 2D bio-based nanomaterial as a green route to amplify the formation of hydrate phases of cement composites: Atomistic simulations and analytical characterization, Constr. Build. Mater. 299 (2021) 123867. https://doi.org/10.1016/j.conbuildmat.2021.123867.

[28] B.S. EN, 197-1: 2011 Cement, Compos. Specif. Conform. Criteria Common Cem. (2011).

[29] A. ASTM, C305-20. Standard practice for mechanical mixing of hydraulic cement pastes and mortars of plastic consistency, ASTM Int. (2020).

[30] P. Payakaniti, S. Pinitsoontorn, P. Thongbai, V. Amornkitbamrung, P. Chindaprasirt, Electrical conductivity and compressive strength of carbon fiber reinforced fly ash geopolymeric composites, Constr. Build. Mater. 135 (2017) 164–176. https://doi.org/10.1016/j.conbuildmat.2016.12.198.

[31] R. Dubey, P. Kumar, Effect of Fly Ash on Water/Powder Ratio and Superplasticizer Dosage in Self-Compacting Mortars, Int. J. Archit. Eng. Constr. (2013) 55–62. https://doi.org/10.7492/ijaec.2013.006.

[32] F. Collins, J. Lambert, W.H. Duan, The influences of admixtures on the dispersion, workability, and strength of carbon nanotube-OPC paste mixtures, Cem. Concr. Compos. 34 (2012) 201–207. https://doi.org/10.1016/j.cemconcomp.2011.09.013.

[33] I. Şanal, N. Özyurt Zihnioılu, A. Hosseini, Particle image velocimetry (PIV) to evaluate fresh and hardened state properties of self compacting fiber-reinforced cementitious composites (SC-FRCCs), Constr. Build. Mater. 78 (2015) 450–463. https://doi.org/10.1016/j.conbuildmat.2014.12.026.

[34] A. ASTM, Standard test method for compressive strength of hydraulic cement mortars (using 2-in. or [50-mm] cube specimens), Annu. B. ASTM Stand. B. ASTM Stand. 4 (2013) 1–9.

[35] B.S. 12390-2-2009 EN, Testing hardened concrete–Part 6: tensile splitting strength of test specimens, London Br. Stand. Inst. (2009).

[36] C. ASTM, Standard test method for flexural strength of concrete (using simple beam with third-point loading), in: Am. Soc. Test. Mater., 2010: pp. 12959–19428.

[37] D.R. RILEM, Determination of the fracture energy of mortar and concrete by means of three-point bend tests on notched beams, Mater. Struct. 18 (1985) 285–290.

[38] Y. Hu, D. Luo, P. Li, Q. Li, G. Sun, Fracture toughness enhancement of cement paste with multi-walled carbon nanotubes, Constr. Build. Mater. 70 (2014) 332–338.

[39] M. Sain, S. Panthapulakkal, Bioprocess preparation of wheat straw fibers and their characterization, Ind. Crops Prod. 23 (2006) 1–8.

[40] A. Kaushik, M. Singh, Isolation and characterization of cellulose nanofibrils from wheat straw using steam explosion coupled with high shear homogenization, Carbohydr. Res. 346 (2011) 76–85.

[41] A. Alemdar, M. Sain, Isolation and characterization of nanofibers from agricultural residues–Wheat straw and soy hulls, Bioresour. Technol. 99 (2008) 1664–1671.

[42] W. Chen, H. He, H. Zhu, M. Cheng, Y. Li, S. Wang, Thermo-responsive cellulose-based material with switchable wettability for controllable oil/water separation, Polymers (Basel). 10 (2018) 592.

[43] R.L. Oliveira, J.G. Vieira, H.S. Barud, R. Assunção, G. R Filho, S.J.L. Ribeiro, Y. Messadeqq, Synthesis and characterization of methylcellulose produced from bacterial cellulose under heterogeneous condition, J. Braz. Chem. Soc. 26 (2015) 1861–1870.

[44] B. Abderrahim, E. Abderrahman, A. Mohamed, T. Fatima, T. Abdesselam, O. Krim, Kinetic thermal degradation of cellulose, polybutylene succinate and a green composite: comparative study, World J. Environ. Eng. 3 (2015) 95–110.

[45] M. Li, L.J. Wang, D. Li, Y.L. Cheng, B. Adhikari, Preparation and characterization of cellulose nanofibers from de-pectinated sugar beet pulp, Carbohydr. Polym. 102 (2014) 136–143. https://doi.org/10.1016/j.carbpol.2013.11.021.

[46] J. Gong, J. Li, J. Xu, Z. Xiang, L. Mo, Research on cellulose nanocrystals produced from cellulose sources with various polymorphs, RSC Adv. 7 (2017) 33486–33493. https://doi.org/10.1039/c7ra06222b.

[47] K.S. Salem, N.K. Kasera, M.A. Rahman, H. Jameel, Y. Habibi, S.J. Eichhorn, A.D. French, L. Pal, L.A. Lucia, Comparison and assessment of methods for cellulose crystallinity determination, Chem. Soc. Rev. (2023) 6417–6446. https://doi.org/10.1039/d2cs00569g.

[48] G. Cheng, P. Varanasi, C. Li, H. Liu, Y.B. Melnichenko, B.A. Simmons, M.S. Kent, S. Singh, Transition of cellulose crystalline structure and surface morphology of biomass as a function of ionic liquid pretreatment and its relation to enzymatic hydrolysis, Biomacromolecules. 12 (2011) 933–941. https://doi.org/10.1021/bm101240z.

[49] H. Seddiqi, E. Oliaei, H. Honarkar, J. Jin, Cellulose and its derivatives : towards biomedical applications, Springer Netherlands, 2021. https://doi.org/10.1007/s10570-020-03674-w.

[50] X. Li, Y.M. Liu, W.G. Li, C.Y. Li, J.G. Sanjayan, W.H. Duan, Z. Li, Effects of graphene oxide agglomerates on workability, hydration, microstructure and compressive strength of cement paste, Constr. Build. Mater. 145 (2017) 402–410. https://doi.org/10.1016/j.conbuildmat.2017.04.058.

[51] Y. Suo, R. Guo, H. Xia, Y. Yang, B. Zhou, Z. Zhao, A review of graphene oxide/cement composites: Performance, functionality, mechanisms, and prospects, J. Build. Eng. 53 (2022) 104502. https://doi.org/10.1016/j.jobe.2022.104502.

Figures

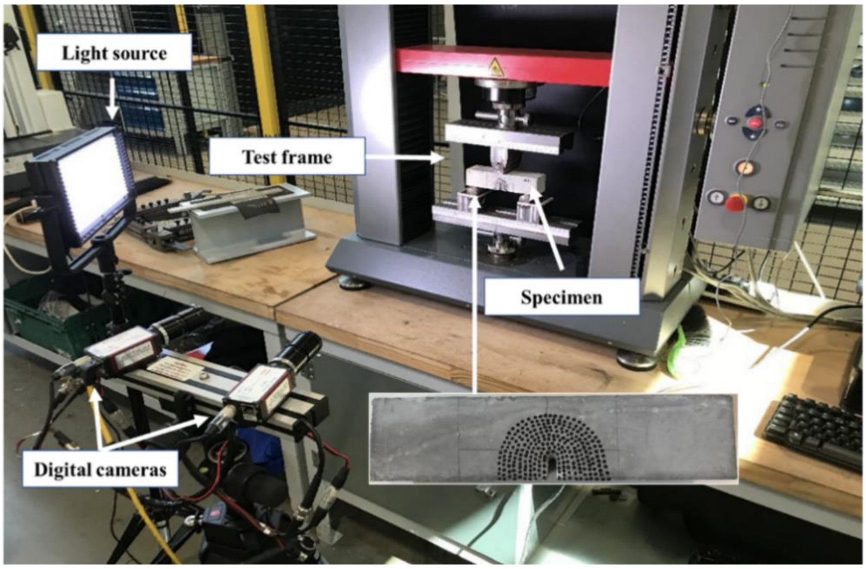

Fig. 1. Three-point bending setup with a video recording system for fracture tests.

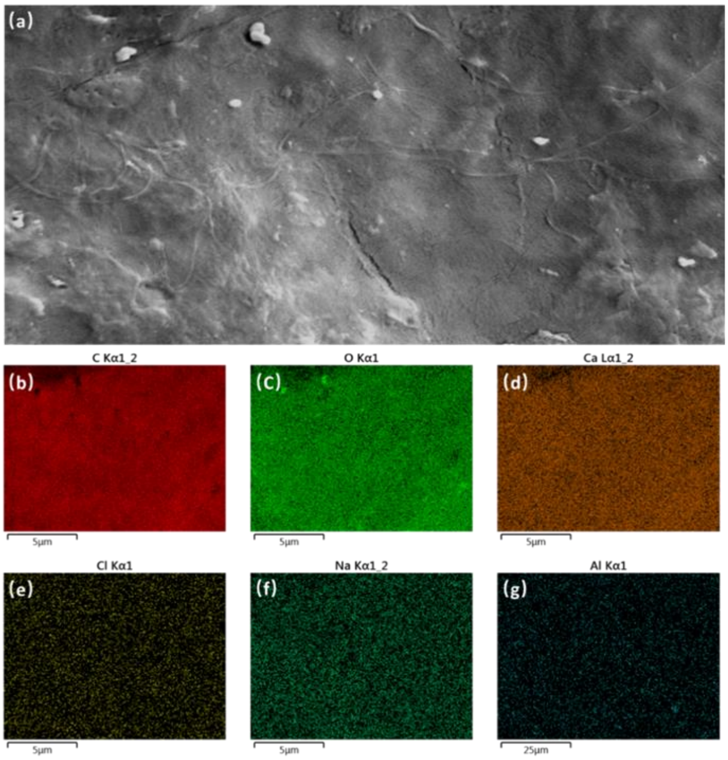

Chemical elements	O	C	Ca	Cl	Na	Al	Mg
Amount (%)	43.1	54.4	1.3	0.6	0.4	0.2	0.1

Fig. 2. SEM of SNS and EDX elemental mapping analysis of SNS (a) SEM image, (b) distribution of carbon element, (c) distribution of oxygen element, (d) distribution of calcium element, (e) distribution of chlorine element, (f) distribution of sodium, (g) distribution of aluminum element

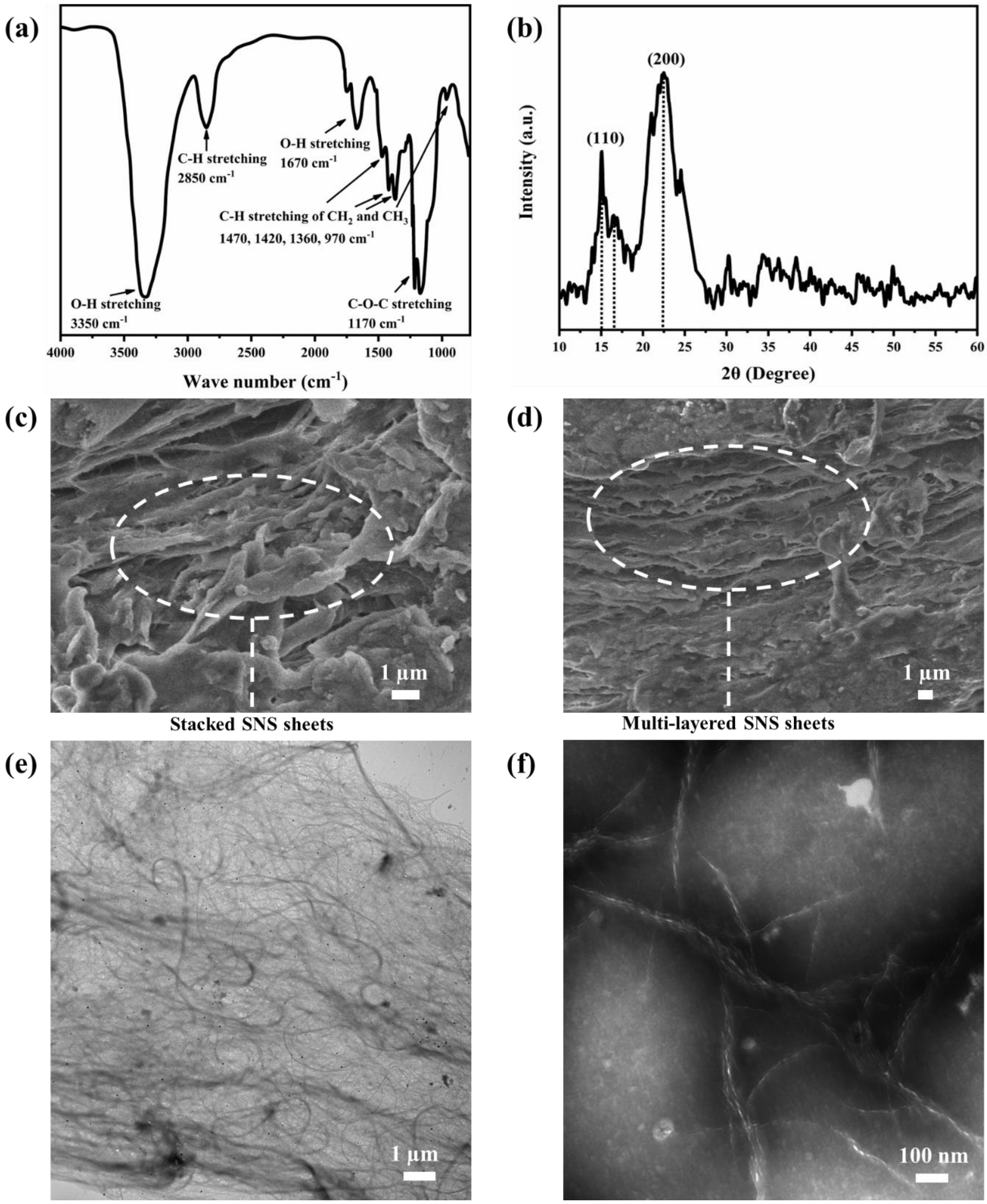

Fig. 3. Functional groups, crystal structure and morphology of SNS (a) FTIR spectrum, (b) XRD spectrum, (c-d) SEM images, (e-f) TEM images of SNS.

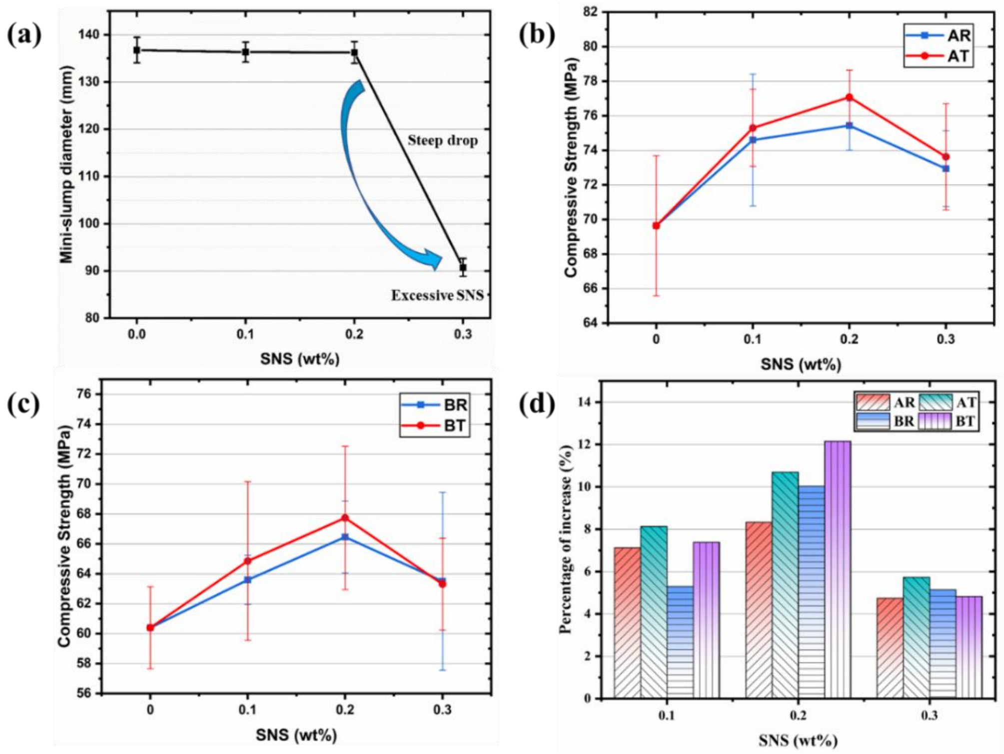

Fig. 4. Workability and compressive strength at 28 days (a) mini-slump workability, (b) compressive strength at a w/c ratio of 0.35, (c) compressive strength at a w/c ratio of 0.45, (d) percentage increases.

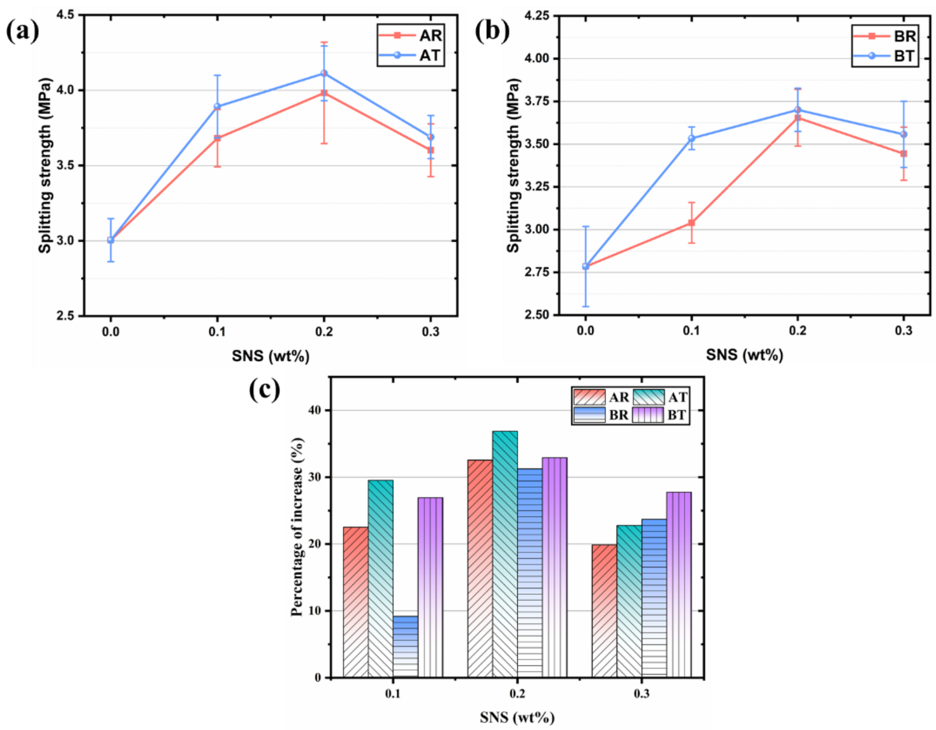

Fig. 5. Splitting tensile strength of cementitious composites at 28 days (a) as received and treated SNS with a w/c ratio of.35, (b) as received and treated SNS with a w/c ratio of 0.4, (c) percentage increases.

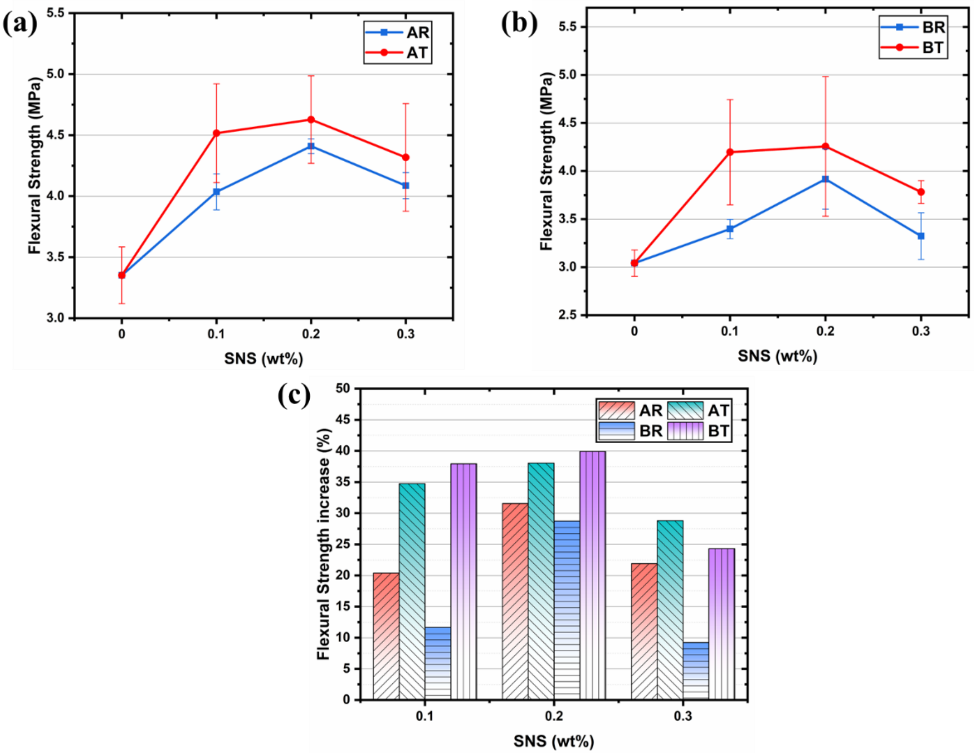

Fig. 6. Flexural strength of cementitious composites at 28 days (a) as received and treated SNS with a w/c of.35, (b) as received and treated SNS with a w/c of 0.4, (c) percentage increases.

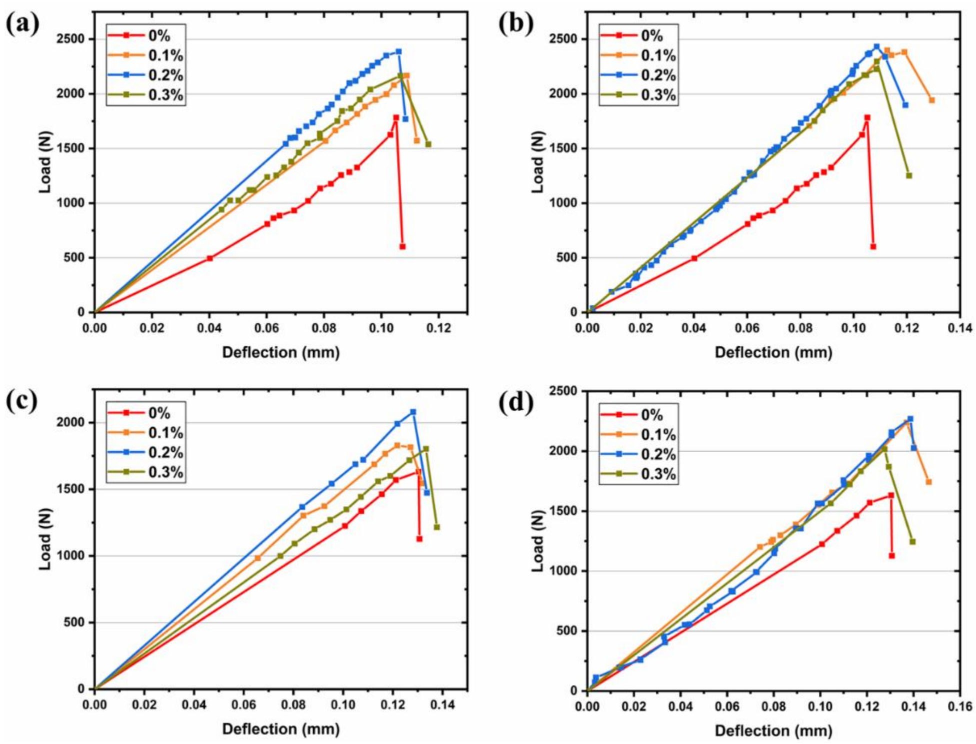

Fig. 7. Flexural load vs deflection curves of cementitious composites s at 28 days (a) as-received SNS with a w/c ratio of 0.35, (b) treated SNS with w/c ratio of 0.35, (c) as-received SNS with w/c ratio of 0.4, (d) treated SNS with a w/c ratio of 0.4.

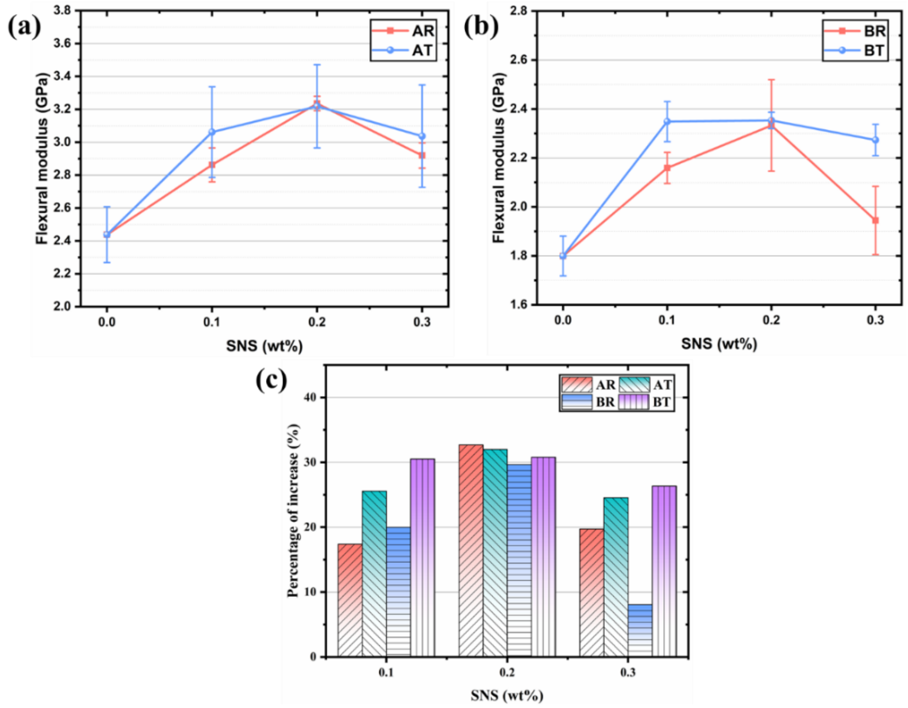

Fig. 8. Flexural modulus of cementitious composites at 28 days (a) as received and treated SNS with a w/c ratio of.35, (b) as received and treated SNS with a w/c ratio of 0.4, (c) percentage increases.

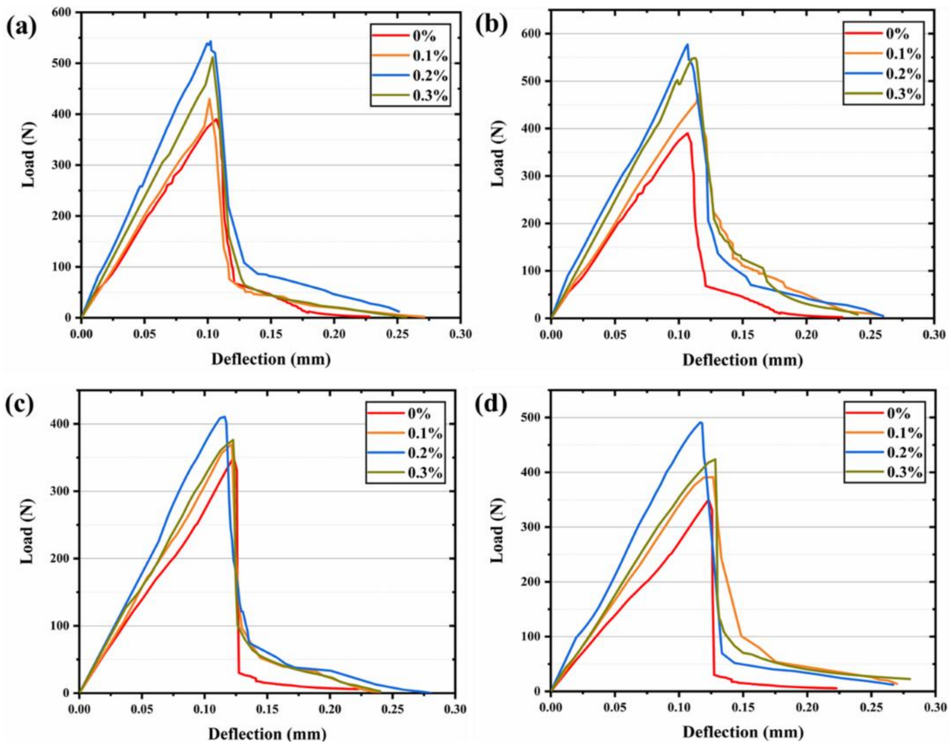

Fig. 9. P vs δ curves of cementitious composites at 28 days (a) as-received SNS with a w/c ratio of 0.35, (b) treated SNS with a w/c ratio of 0.35, (c) as-received SNS with a w/c ratio of 0.4, (d) treated SNS with a w/c of ratio 0.4.

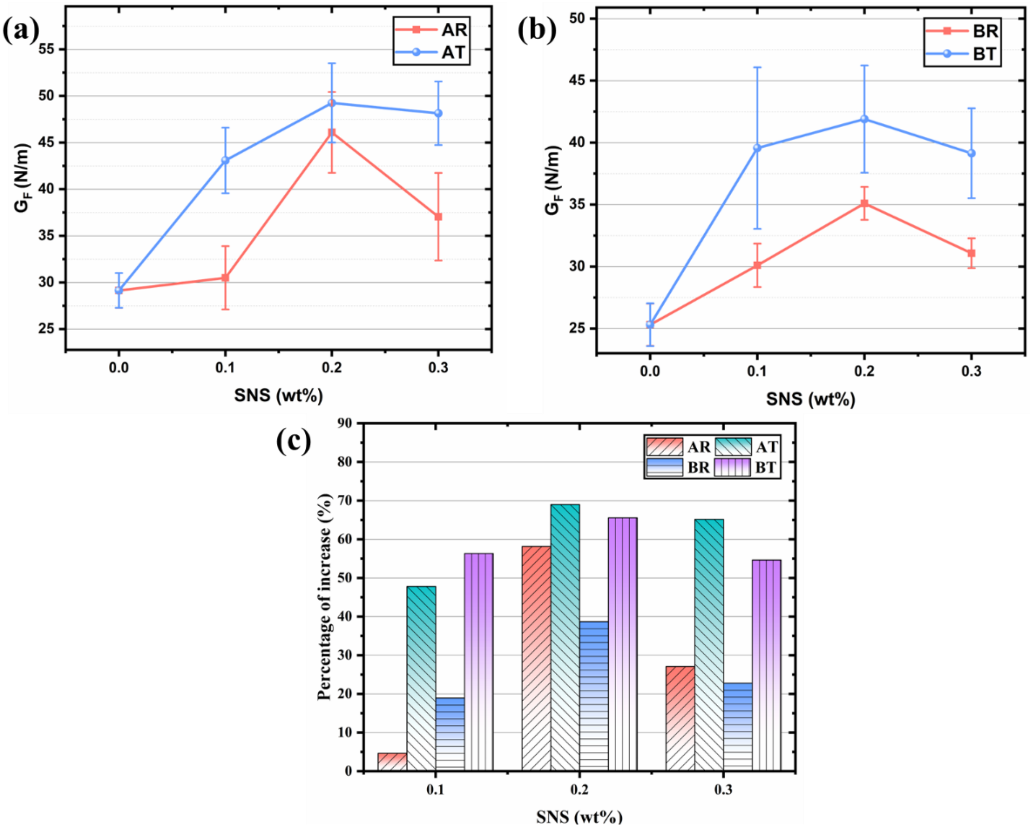

Fig. 10. Fracture energy at 28 days (a) with as received and treated SNS at a w/c of.35, (b) with as received and treated SNS at a w/c of 0.4, (c) percentage increases.

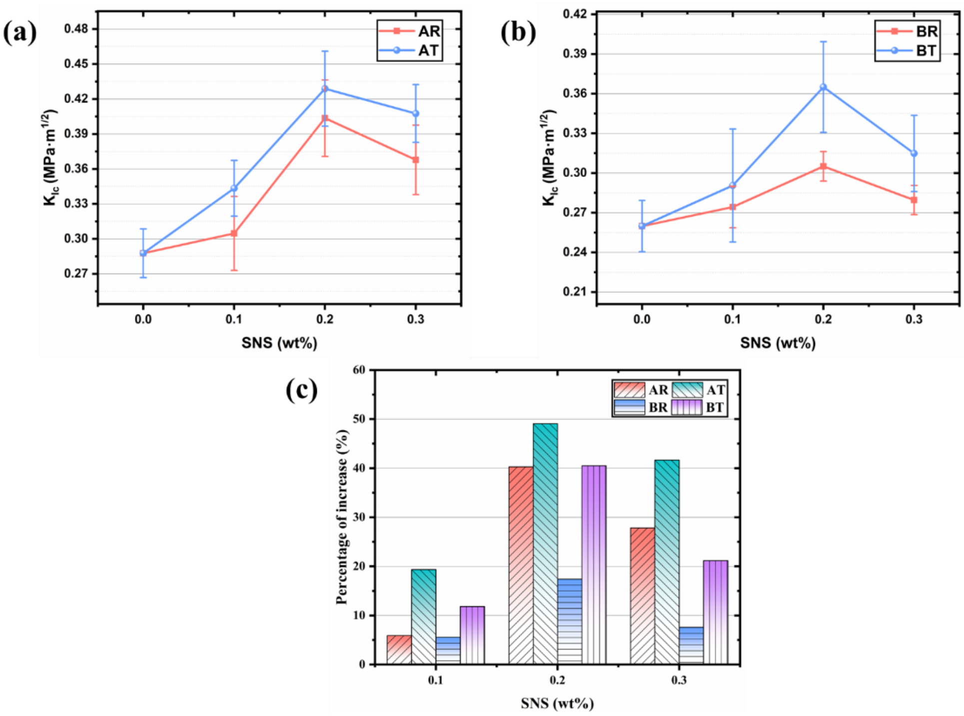

Fig. 11. Fracture toughness of cementitious composites at 28 days (a) as received and treated SNS with a w/c ratio of.35, (b) as received and treated SNS with a w/c ratio of 0.4, (c) percentage increases.

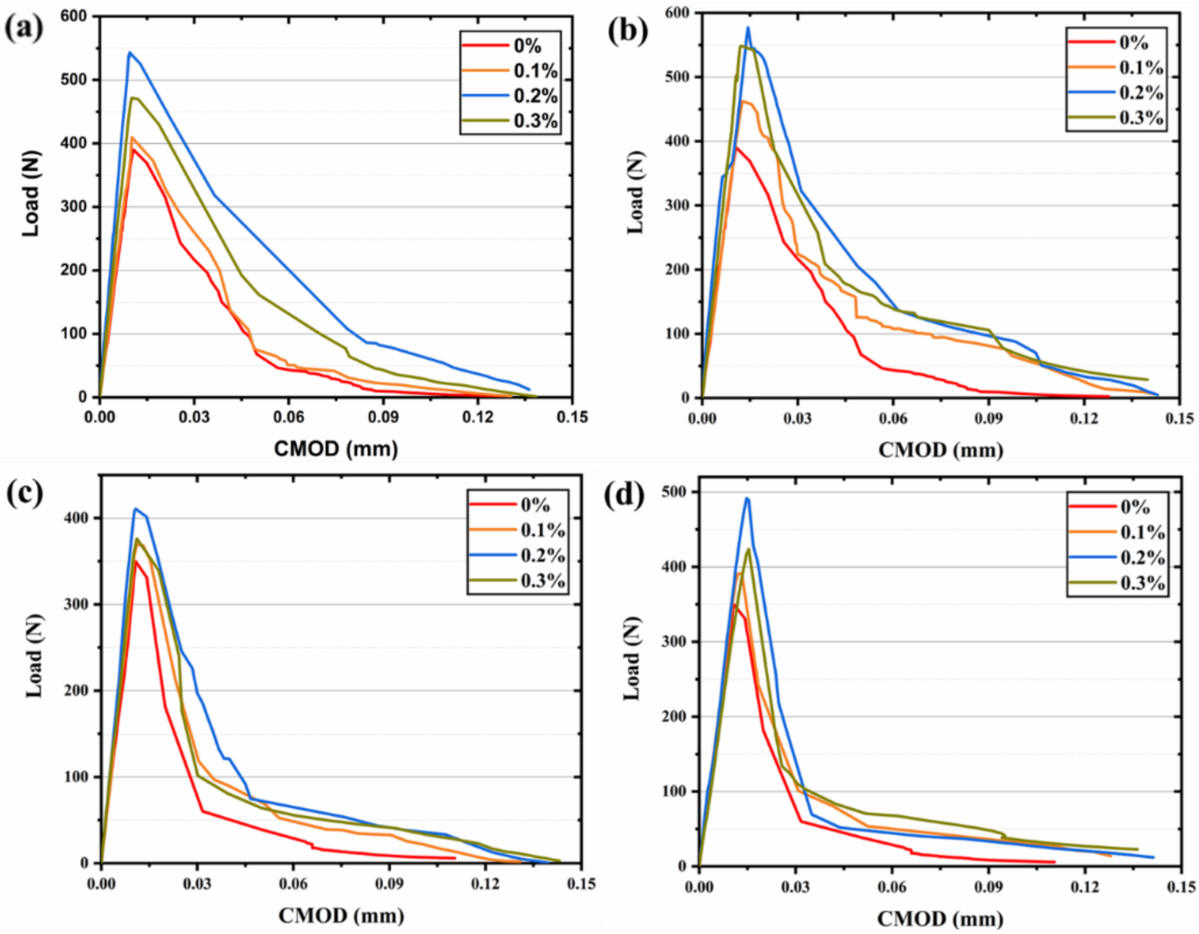

Fig. 12. Load-CMOD curves of cementitious composites. (a) as-received SNS with a w/c ratio of 0.35, (b) treated SNS with a w/c ratio of 0.35, (c) as-received SNS with a w/c ratio of 0.4, (d) treated SNS with a w/c of ratio 0.4

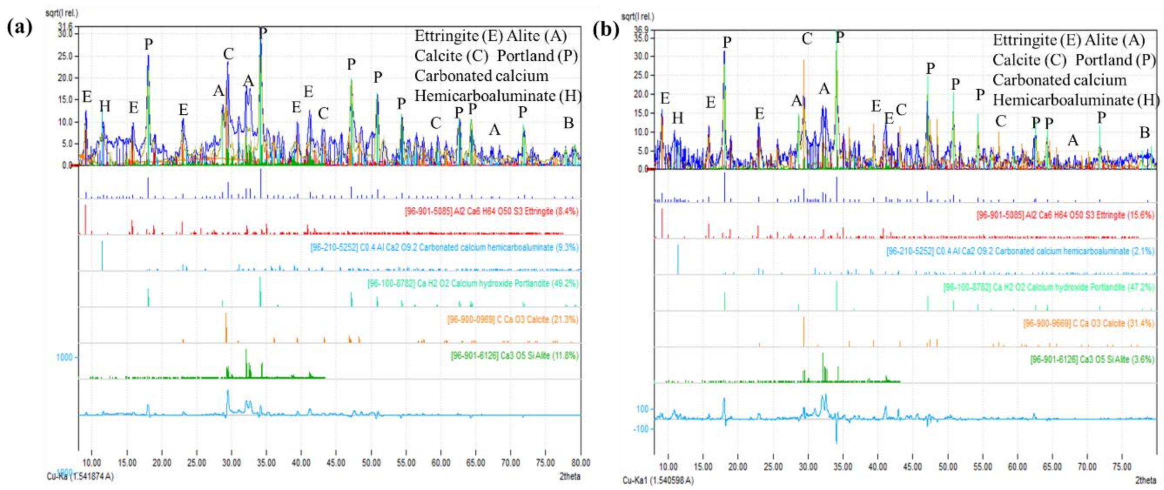

Fig. 13. XRD analysis of cementitious composites at 28 days (a) with 0 -wt% SNS, (b) with 0.3 -wt% SNS.

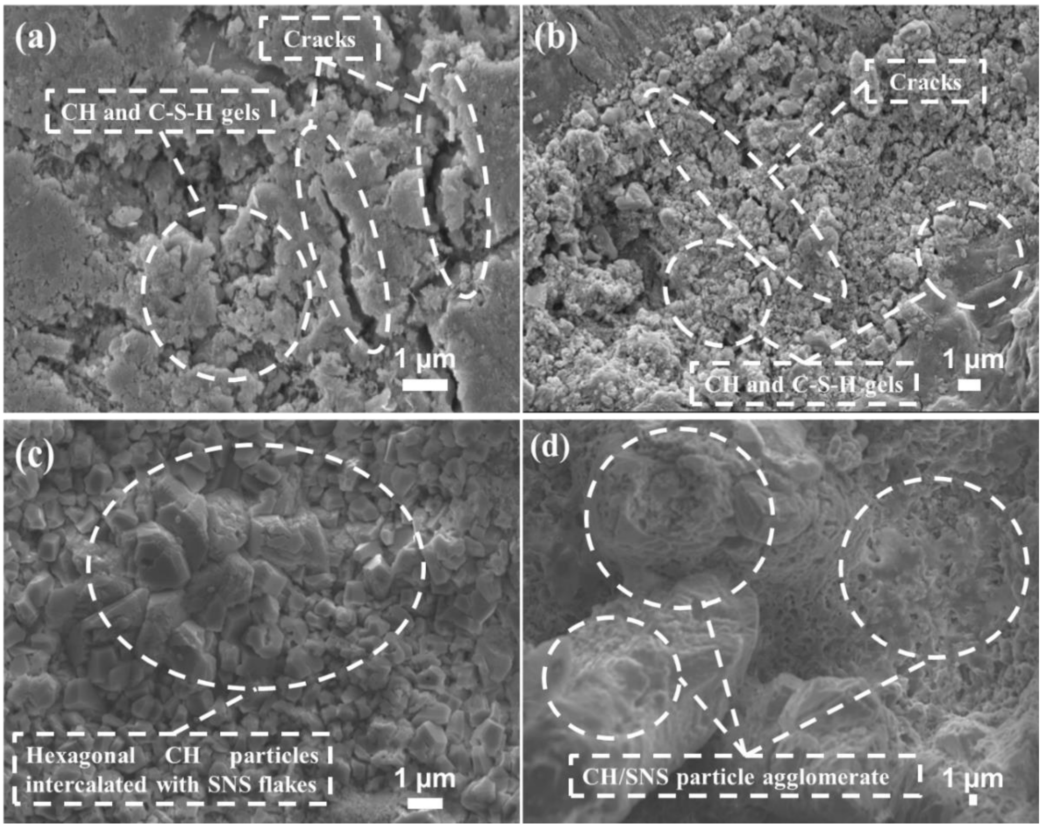

Fig. 14. SEM micro images of cementitious composites at 28 days (a) plain cementitious composite, (b) with 0.1-wt% treated SNS, (c) with 0.2-wt% treated SNS, (d) with 0.3-wt% treated SNS**.**

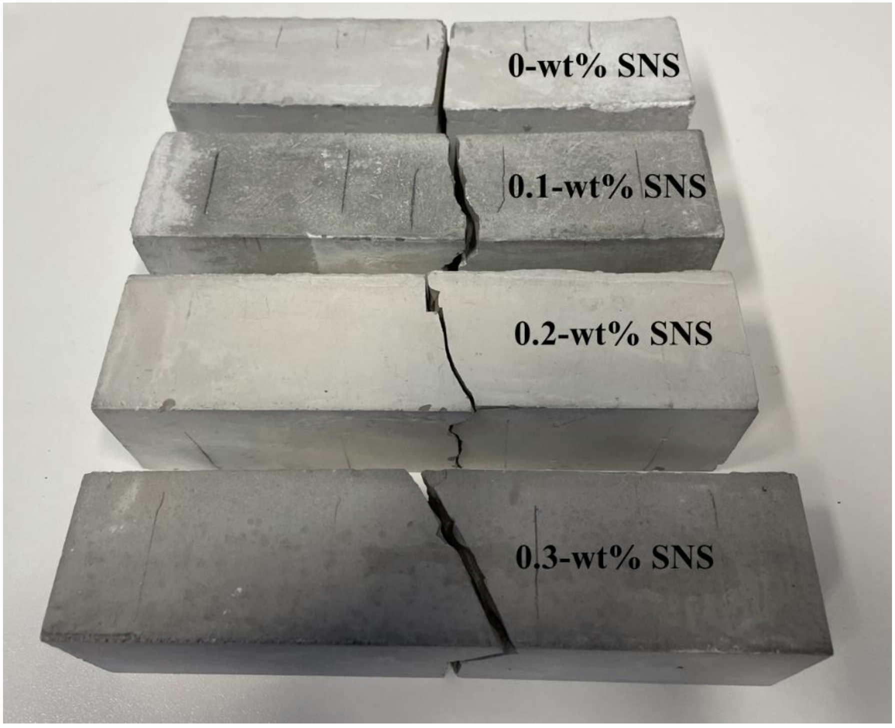

Fig. 15. Failure modes showing crack deflection mechanism in SNS reinforced cement prisms.

Tables

Table 1

Physical properties of OPC

Main particle size	pH	Relative density	Apparent density	Solubility in water
5-30 µm	11-13.5	2.75-3.20	0.9-1.5 g/cm³	Slight (0.1-1.5 g/l)

Table 2

Chemical components of OPC

Composition	SiO_2	Al_2O_3	Fe_2O_3	*CaO*	*MgO*	SO_3	K_2O	Na_2O	*Cl*
Amount (%)	20.85	5.22	2.25	64.98	2.40	3.37	0.61	0.27	0.05

Table 3

Mixture proportions of SNS platelet reinforced paste

Mix No.	Unit weight						
	Cement (g)	Water (g)	SP (g)	SNS(R) (g)	SNS(T) (g)	W/C ratio	SNS (wt%)
AP00	300	105.00	3	0.00	0.00	0.35	0.00
AR01	300	105.00	3	0.30	0.00	0.35	0.10
AR02	300	105.00	3	0.60	0.00	0.35	0.20
AR03	300	105.00	3	0.90	0.00	0.35	0.30
AT01	300	105.00	3	0.00	0.30	0.35	0.10
AT02	300	105.00	3	0.00	0.60	0.35	0.20
AT03	300	105.00	3	0.00	0.90	0.35	0.30
BP00	300	105.00	3	0.00	0.00	0.40	0.00
BR01	300	105.00	3	0.30	0.00	0.40	0.10
BR02	300	105.00	3	0.60	0.00	0.40	0.20
BR03	300	105.00	3	0.90	0.00	0.40	0.30
BT01	300	105.00	3	0.00	0.30	0.40	0.10
BT02	300	105.00	3	0.00	0.60	0.40	0.20
BT03	300	105.00	3	0.00	0.90	0.40	0.30

P: plain cement, R: as-received SNS and T: treated SNS.

Responses to reviewers' comments

Journal: Construction and Building Materials
Manuscript number: CONBUILDMAT-D-22-11953R2
Title: Mechanical and fracture properties of sugar beetroot-based nanosheets (SNS) doped cementitious composites
Authors: *Bo Huang, Yin Chi, Jianqun Wang, Gongxun Wang, Junjie Ye, Eric Whale, David Hepworth, Jianqiao Ye, Mohamed Saafi*

The authors would like to thank the reviewers for their valuable comments and editorial suggestions. All the comments have been addressed in the revised manuscript. As suggested by the reviewers, we edited the manuscript to improve its content and legibility. A detailed list of the point-by-point responses to the comments is given below. The basic format follows the sequence: Comments, Reply and Corrections. The revised text is highlighted in blue for easy identification.

Responses to Reviewer #1

No.	Comments, Reply and Corrections	
1.	Comments	*I don't have any other comments.*
	Reply	We thank the reviewer for reviewing our manuscript.
	Corrections	No specific changes were made in the text.

Responses to Reviewer #2

No.	Comments, Reply and Corrections	
1.	Comments	*thank you very much for having accepted the suggested corrections. However, I invite you to check again the Segal's equation (equation 5) where the index "002" is not the right one and should be "200" because the peak at 2θ=22.5° is the (200) one (see, for example: Chem. Soc. Rev., 2023, 52, 6417).*
	Reply	Correction was made in Section 3.1.
	Corrections	(1) In Section 2.1, the character "I_{002}" now reads: "I_{200}"; the character "I_{am}" now reads: "I_{AM}". (2) The reference *"M.M. Rana, H. De la Hoz Siegler, Influence of ionic liquid (IL) treatment conditions in the regeneration of cellulose with different crystallinity, J. Mater. Res. 38 (2023) 328–336. https://doi.org/10.1557/s43578-022-00797-7."* now reads: "K.S. Salem, N.K. Kasera, M.A. Rahman, H. Jameel, Y. Habibi, S.J. Eichhorn, A.D. French, L. Pal, L.A. Lucia, Comparison and assessment of methods for cellulose crystallinity determination, Chem. Soc. Rev. (2023) 6417–6446. https://doi.org/10.1039/d2cs00569g.".
2.	Comments	** page 11, line20: "The diffraction peak at 2 =22.5° were attributed" should be: "The diffraction peak at 2 = 22.5° was attributed",*

	Reply	Correction was made in Section 2.1.
	Corrections	In Section 3.1, the sentence *"The diffraction peak at 2θ =22.5° were attributed…"* now reads: "The diffraction peak at 2θ =22.5 ° was attributed…".
3.	Comments	** Figure 13: Rietveld refinements are accurate when you identify all the phases. You should index the peak at 2 = 11.5-12° and estimate again the different phases content. This phase could be a C-A-H one, like Calcium Aluminum Oxide Carbonate Hydrate (C3A.CaCO3.11H2O, JCPDF card n°41-0219), for example.*
	Reply	We identified carbonated calcium hemicarboaluminate (C0.4AlCa2O9.8) as a phase at 2θ= 11.5-12°. All corrected the Rietveld refinements are in Section 3.5.
	Corrections	(1) We added the following sentence within Section 3.5."carbonated calcium hemicarboaluminate (COD 96-210-5252).". (2) In Section 3.5, the sentence *"The results of the Rietveld refinements shown in Fig. 13, demonstrate that the quantity of $Ca(OH)_2$ and $CaCO_3$ have increased from 28.5% and 18.9% to 40.8% and 36.2%, respectively. The amount of ettringite has decreased from 26.6% to 21.0%, while the content of alite has decreased to 2%."* now reads: "The results of the Rietveld refinements shown in Fig. 13, demonstrate that the quantity of ettringite and $CaCO_3$ have increased from 8.4% and 21.3% to 15.6% and 31.4%, respectively. The amount of $Ca(OH)_2$ has decreased from 49.2% to 47.2%, while the content of alite and carbonated calcium hemicarboaluminate has decreased to 3.6% and 2.1%.". (3) We have updated the following Fig. 13 within Section 3.5. 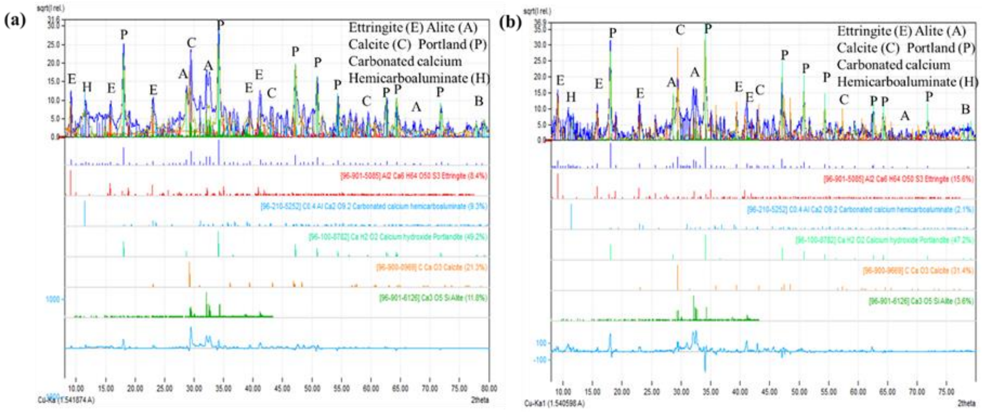 Fig. 13. XRD analysis of cementitious composites at 28 days (a) with 0 -wt% SNS, (b) with 0.3 -wt% SNS.

Highlights

- Treated and non-treated SNS flakes enhanced the mechanical and fracture properties of the cementitious composites.
- The SNS strengthening and toughening mechanisms in the cementitious composites are crack bridging and crack deflection.
- The SNS induced performance enhancement similar to that of graphene-based materials.

Mechanical and fracture properties of sugar beetroot-based nanosheets (SNS) doped cementitious composites

Bo Huang [a,b], Yin Chi [c*], Jianqun Wang [a], Gongxun Wang [a], Junjie Ye [d], Eric Whale [e], David Hepworth [e], Jianqiao Ye [b], Mohamed Saafi [b*]

[a] School of Civil Engineering, Hunan University of Science and Technology, Xiangtan, 411201, China
[b] Department of Engineering, Lancaster University, Lancaster LA1 4YW, UK
[c] School of Civil Engineering, Wuhan University, Wuhan, 430072, China
[d] Research Center for Applied Mechanics, Key Laboratory of Ministry of Education for Electronic Equipment Structure Design, Xidian University, Xi'an 710071, China
[e] Cellucomp Ltd, Burntisland, Fife KY3 9DW, UK

Abstract

This paper examines the mechanical and fracture properties of cementitious composites doped with a new type of 2D bio-nanoplatelets sheets, synthesized from sugar beet pulp waste. The sugar beetroot nanosheets (SNS) were added to the cement pastes at different concentrations. The influence of SNS treatment and water-to-cement (w/c) ratio on the performance of the cementitious composites was elucidated. The experimental results showed that 0.2-wt% and 0.35 were the optimal SNS concentration and w/c ratio for increasing the compressive, splitting tensile and flexural strength, flexural modulus, fracture energy and fracture toughness. These properties were enhanced by as much as 12.15%, 36.87%, 39.91%, 32.69%, 69.01% and 49.06%, respectively. This enhancement was due to crack deflection and crack bridging mechanisms in the cementitious composites as a result of the high specific surface area of SNS and the strong chemical and physical bonding of SNS with the hydration phases. The SNS materials offers strong advantages over graphene-based materials on improving the engineering properties of cementitious materials and reducing their cost and CO_2 emissions.

Highlights

* Corresponding author. E-mail address: yin.chi@whu.edu.cn (Yin Chi). m.saafi@lancaster.ac.uk (Mohamed Saafi)

- Treated and non-treated SNS flakes enhanced the mechanical and fracture properties of the cementitious composites.
- The SNS strengthening and toughening mechanisms in the cementitious composites are crack bridging and crack deflection.
- The SNS induced performance enhancement similar to that of graphene-based materials.

Key Words

Bio-nanoplatelets; Cementitious composites; Mechanical properties; Fracture properties

1. Introduction

Ordinary Portland Cement (OPC), the key ingredient of concrete, is responsible for 8-9% of the global CO_2 emissions [1]. Because there are no other cementitious materials that can replace OPC in the foreseeable future to meet the need for future physical infrastructure, its global demand is forecasted to increase by about 50% by 2050 [2,3], resulting in significant increase in CO_2 emissions. One of the popular approaches to reduce the consumption of OPC-based materials involves the use of the so-called "do more with less" method where different types of additives are added to cementitious materials to improve their engineering properties. As a result, smaller size structural members can be designed which in return reduces both the volume of concrete and the demand for OPC.

Various types of macro fibers have been employed to improve the engineering properties of cementitious composites. For example, high-strength steel, polypropylene polyvinyl alcohol (PVA), polyethylene glycol (PEG) and carbon fibers were commonly used to enhance the mechanical and fracture properties of cementitious composites [4–9].

Micro and nanofibers were found to outperform macrofibers for improving the microstructure and overall mechanical properties of cementitious composites. Owing to their chemical functional groups and small size, carbonaceous materials such as carbon nanotubes

(CNTs), graphene and graphene oxide (GO) promote the hydration of the cement particles which in return increases the amount of the calcium silicate hydrate (C-S-H) phases [10–15]. These materials also strengthen the hydration phases. Unlike CNTs, the high specific surface area of graphene and GO materials creates stronger and more crack resistant cementitious composites [16,17].

The large-scale application of CNTs, graphene and GO in cementitious materials however is limited. This is because these carbonaceous materials are expensive, their production is energy intensive and pose serious health and safety issues [18]. In addition, they are incompatible with cementitious materials as they tend to agglomerate in water thus degrading their mechanical properties [19]. Bio-based materials are considered as a low-cost and sustainable alternative to micro and nanofibers. Previous research has shown that cellulose nanofibers (CNFs) and cellulose nanocrystals (CNCs) [20,21] chemically interact with cement, thereby improving its hydration kinetics. Because of this, CNFs and CNCs help improve the formation and growth of the hydration phases [22]. However, CNFs and CNCs have moderate effect on the mechanical and fracture properties of cementitious composites due to their small specific surface area [23].

Therefore, there is a genuine need for new low cost and environmentally friendly materials as alternatives to graphene, GO, CNT, CNF and CNC reinforcing materials. Recently, we successfully synthesized 2D SNS flakes for applications in cementitious composites. Compared with graphene-based materials, SNS has higher specific surface area and richer in chemical hydroxyl functional groups which enables the SNS flakes to chemically interact with both the cement particles during hydration and the produced hydration phases [24,25]. The SNS material is also significantly cheaper than graphene-based materials and its production is scalable for large deployment in the construction industry. Our Density Functional Theory (DFT) and Molecular Dynamics (MD) simulations and Electrochemical (EC) characterization have shown that the SNS flakes significantly improve the hydration kinetics of cement and increases the mechanical properties of C-S-H globules [26,27]. However, the strengthening and toughening mechanisms in SNS doped cementitious composites are not yet fully understood and the resulting macro engineering properties are still unknown. As such, this paper aims to elucidate the role of the SNS flakes in improving the mechanical and fracture properties of cementitious. An extensive experimental program was carried out to determine the influence of SNS on the compressive, tensile, and flexural strength, flexural modulus, fracture energy and fracture toughness of the cementitious composites. The experimental parameters considered in this program were SNS concentration (0, 0.1, 0.2, 0.3-wt%), SNS treatment (sonicated and non-sonicated) and w/c ratio (0.35 and 0.40).

2. Experimental program

2.1 Materials

Ordinary Portland Cement (OPC), CEM I 52.5R (Hanson, UK) was used to prepare the cement pastes. Table 1 and Table 2 list the OPC physical properties and chemical composition. The main components of OPC are CaO (64.98%), SiO_2 (20.85%) and Al_2O_3 (5.22%) with a particle size ranging from 5 to 30 μm and a relative density of 2.75-3.20. These properties meet the requirements of B.S EN 197-1:2011 standard [28]. A Polycarboxylic ether-based superplasticizer (SP) (MasterGlenium®51, BASF, UK) was used at a concentration of 1-wt% to improve the workability of the cement pastes. The SNS flakes were synthesized by our industrial partner, Cellucomp Limited (UK). The SNS flakes are 50 μm in width, 50 μm in length and 0.25 μm in thickness. And their specific surface area and density are 68.35 m^2/g and 1.31g/cm^3, respectively.

The manufacturing process for the SNS flakes is described in [26,27]. The first step in this process involved diluting the sugar beet pulp with a solid content of 1% by weight.

Subsequently, the pH of the solution was increased to 14 using 0.5 M sodium hydroxide (NaOH). The NaOH was purchased from Honeywell Fluka™ and a purity of 98%. This enables the removable of the hemicellulose and pectin from the mixture. The mixture was then thermally treated at 90 ℃ for 5 hours and periodically homogenized for 1 hour with a stirring blade rotating at 700 rpm. At the end of the thermal treatment, the mixture was homogenized for 5 minutes at 1900 rpm. The SNS mixture was then filtered and a SNS paste with a solid content of 4 to 8-wt%was obtained.

2.2 Mix proportions and specimen preparation

The mix proportions adopted in this study were divided into two groups (groups A and B) as shown in Table 3. In all groups, the cement pastes were doped with SNS at concentrations of 0.0, 0.1, 0.2 and 0.3-wt%. In group A, cement pastes with a w/c ratio of 0.35 were doped with as-received SNS (samples AR) and treated SNS (samples AT). In group B, the cement pastes with a w/c ratio of 0.4 were doped with as-received SNS (samples BR) and treated SNS (samples BT). The samples AP in group A and BP in group B were used as plain samples for reference purposes. The treatment of SNS consisted of sonicating the SNS solution for 30 minutes. In this treatment process, the required amount of SNS was first added to the required amount of water and SP. Subsequently, the solution was sonicated in an ice bath with a sonifier (Branson Sonifier 450) at 50% duty cycles. The as-received SNS solution was prepared by manually stirring the mixture of the required amount of SNS, water and SP.

The cement pastes were prepared according to ASTM C305-20 [29]. The cement powder and the SNS solution were first mixed for 30 seconds at a mixing speed of 140 revolutions/min, then mixed for 120 seconds at a mixing speed of 285 revolutions/min until the SNS flakes were evenly dispersed in the fresh cement paste. The cement pastes were poured into 40 mm x 40 mm x 160 mm and 50 mm x 50 mm x 50 mm steel molds. The molds were placed on a vibrating table and vibrated for 60 seconds. The molds were covered with a plastic film to prevent water evaporation and left to cure at room temperature for 24 hours. The samples were then demolded and placed in a standard curing tank with water temperature of 20±2℃ until testing.

2.3 Workability and mechanical properties

A mini-slump test was conducted to determine the influence of the SNS flakes on the workability of the cement pastes. This was done by measuring the spread diameters formed by the pastes upon lifting the mini-slump cone [30,31]. The top and bottom diameters and the height of the cone are 70 mm, 100 mm and 60 mm, respectively. The workability of the cement pastess was measured according to [32]. The workability W of the cement pastes was determined using the following equation [33]:

$$\mathrm{W} = \left(\frac{\frac{(d_1 + d_2)}{2} - d_0}{d_0} \right) \times 100 \quad (1)$$

where d_1 and d_2 are the two direction spread-out diameters of the paste and d_0 is the bottom diameter of the cone.

The mechanical properties were determined at 28 days of curing. The compressive strength of the cementitious composites was determined according to ASTM C 109 standard [34]. A total of 56 cubes (50 mm in side) were tested using a universal testing machine (UTM, 250 kN) at a loading rate 0.5 MPa/s. The splitting tensile strength of the cementitious composites was evaluated according to BS EN12390-6:0229 [35] using UTM. A total of 42 cylinders (100 mm x 200 mm) were tested with a loading rate of 0.06 MPa/s. A total of 56 prisms (40 mm x 40 mm x 160 mm) were subjected to four-point bending test according to ASTM C78 [36] using UTM at loading rate of 0.5 MPa/s to determine the flexural strength and flexural modulus of the cementitious composites.

2.4 Fracture properties

The fracture properties of the cementitious composites were evaluated using the three-point bending test method according to the RILEM standard (1985). A total of 56 notched prisms (40 mm ×40 mm × 160 mm) were tested using UTM at a displacement rate of 0.02 mm/min. The notch depth and height are 3 mm and 16 mm, respectively. As shown in Fig.1, during loading, the crack mouth opening displacement (CMOD) was measured with a video gauge™ (Imetrum Ltd). The video gauge consisted of two camera lenses, an Imetrum controller and a computer data acquisition system. Uniform black dots were printed on the surface of the prism around the notch. The printed area defines the region where the displacement is measured. To capture the positions of the dots during testing, the lenses were placed 1.2 m from the prism surface. The load, prism deflection and positions of the dots were recorded at a frequency 15 Hz. The CMOD was obtained by monitoring the horizontal displacement between the two dots adjacent to the mouth of the crack. This was achieved by collecting measurements generated by the video gauge in the form of pixel displacement. During testing, a series of pixel displacement results was recorded and the pixel displacement was then converted to real displacement in mm by the data acquisition system software.

The measured applied load (P), deflection (δ) and CMOD were used to calculate the fracture energy (G_F) and fracture toughness (K_{IC}) using the following equations [38].

$$G_F = \frac{mg\delta_0 + W_0}{t(h-a)} = \frac{mg\delta_0 + \delta_0^{\delta_0} P(\delta) d\delta}{t(h-a)} \tag{2}$$

$$K_{IC} = \frac{P_{max} S}{t h^{\frac{3}{2}}} f\left(\frac{a}{h}\right) \tag{3}$$

$$f\left(\frac{a}{h}\right) = 2.9\left(\frac{a}{h}\right)^{\frac{1}{2}} - 4.6\left(\frac{a}{h}\right)^{\frac{3}{2}} + 21.8\left(\frac{a}{h}\right)^{\frac{5}{2}} - 37.6\left(\frac{a}{h}\right)^{\frac{7}{2}} + 38.7\left(\frac{a}{h}\right)^{\frac{9}{2}} \tag{4}$$

where G_F is the fracture energy, m is the mass ($m = m_1 + m_2$), m_1 is the mass of the prism between supports, m_2 is the mass of the loading fixture, g is the gravity acceleration, δ_0 is the final displacement of the failure prism, W_0 is the area under the load-displacement curve, t is the thickness of the prism, h is the height of the prism, a is the depth of the notch, K_{IC} is the fracture toughness, P_{max} is the peak load and S is the span of the prism.

2.5 Characterization of SNS and cementitious composites

The SNS flakes were characterized to determine their functional groups, crystal structure and morphology. The as-received SNS material was dried, and samples were prepared for characterization. Fourier-transform infrared (FTIR) spectrometer (Agilent Technologies ExoScan 4100) was employed to determine the chemical properties of the SNS flakes. The SNS sample was subjected to 128 consecutive scans in the frequency range of 4000-500 cm^{-1} at a spectral resolution of 8 cm^{-1}. The obtained infrared absorption spectrum was used to identify the functional groups of SNS. Single-crystal X-ray diffractometer (XRD) (Agilent SuperNova) was used to analyze the crystal structure of the SNS flakes. The XRD patterns of SNS were recorded in the range of 5° to 65° (2θ) with a scanning rate of 2°/min, with a step size of 0.01°.

Analytical field emission scanning electron microscope (FE-SEM) with an energy dispersive X-ray spectroscopy (EDS/EDX) system (JEOL JSM-7800F) was employed to observe the morphology of the SNS flakes. The EDS/EDX system has a Silicon Drift Detector (SDD) (X-Max50) of an area of 50 mm^2. The SNS sample was coated with gold prior to the characterization then transferred to the instrument vacuum chamber and characterized at an accelerating voltage of 2-15 kV at ambient temperature.

The morphology of the SNS flakes was further evaluated using transmission electron microscope (TEM) (JEM-1010). To generate TEM images of the sample, a SNS solution with a concentration of 0.2-wt% was prepared. The SNS suspension was then dripped onto carbon-coated TEM grids and allowed to air-dry at room temperature. The TEM imaging was then performed at an acceleration voltage of 80 kV.

The microstructure of the cementitious composites was characterized at 28 days. Samples recovered from broken prisms were ground into powder by a planetary ball-mill (grinding machine PM 100) and used to identify the crystal structure of the cementitious composites using XRD. Samples recovered from broken prisms were also polished into small pellets then coated with gold to determine the morphological features of the cementitious composites using SEM/EDX.

3. Experimental results and discussion

3.1 Characterization of SNS

Fig. 2 shows a typical SEM image of the SNS flakes along with their elemental mapping analysis and chemical composition. As shown, the SNS flakes are mainly composed of carbon (54.4%) and oxygen (43.1%). Impurities such as calcium (1.3%), chlorine (0.6%), sodium (0.4%) and aluminum (0.2%) from the preparation process are also shown in Fig. 2. The FTIR spectrum of the SNS flakes is shown in Fig. 3a. The absorbance peak of around 3350 cm^{-1} represents the stretching vibration of the hydroxy group (O-H), which indicates the hydrophilicity of the SNS flakes [39,40]. The prominent peak at 2850 cm^{-1} is due to the stretching and vibration of saturated C-H in cellulose [41]. The peak at 1675 cm^{-1} reflects the stretched O-H groups, which corresponds to the adsorbed water molecules. The 1470, 1420, 1360 and 970 cm^{-1} bands are attributed to C-H stretching of methylene (CH_2) and methyl (CH_3) groups. The signal at 1170 cm^{-1} indicates a C-O-C bond, which is the characteristic of cellulose ethers [42–44]. The functional groups of the SNS flakes provide unique advantages over carbonaceous materials as they allow the SNS flakes to disperse in water and chemically interact with the cement particles and hydration phases, thereby improving the hydration and engineering properties of the cementitious composites.

The XRD pattern of SNS is shown in Fig. 3b. As depicted in this figure, the SNS exhibits diffraction peaks around 2θ=16.5° and 22.5°. This indicates that SNS has typical cellulose-I structural features. The peak at 2θ =16.5° represents the SNS crystalline (110) plane. In this plane, the surfaces of the SNS flakes are decorated with mainly hydroxyl groups with some hydrophilic groups. The hydroxyl groups promote the dispersion of the SNS flakes in water [45]. The diffraction peak at 2θ =22.5° was attributed to the (200) plane where the SNS consists of lignin and hemicellulose [45,46].

The crystallinity index (CI) value obtained from XRD is an indication of how mechanically strong the SNS flakes are. The CI value of the SNS flakes can calculated using the following equation [47]:

$$CI = 100 \times \frac{I_{200} - I_{AM}}{I_{200}} \quad (5)$$

Where I_{200} represents the maximum intensity of the (200) diffraction peak, located around 2θ=22.5°, I_{AM} is the minimum diffraction intensity of the amorphous SNS (2θ=18°) between the 2θ=16.5° and 22.5° [48]. Based on equation (5), the average *CI* value for the SNS flakes is 75.65%. This relatively high *CI* value suggests that the SNS flakes possess high stiffness, rigidity and strength [49].

Fig. 3c-d depict SEM images of the SNS flakes. These images indicate the sample is composed of stacked and overlapped SNS sheets. The SNS sheets display wrinkled, crumpled and rippled features. Graphene based 2D materials also possess these features. The TEM images of the SNS flakes are shown in Fig. 3e-f. The purity of the SNS product is high, which clearly shows that most of the hemicellulose and lignin have been removed during the fabrication process. As can be seen, the SNS flakes are composed of intertwined and randomly oriented cellulose nanofibers with a diameter of about 40 nm.

3.2 *Workability, compressive and tensile strength of SNS cement pastes*

Fig. 4a shows the influence of SNS on the workability of the cement pastes. The workability *W* of the plain cement paste is 136%. As shown, the addition of 0.1 and 0.2-wt% SNS did not affect the workability of the cement pastes significantly. However, the addition of 0.3-wt% SNS reduced the workability of the cement paste by 33.4%.

Fig. 4b-c plot the compressive strengths of the cementitious composites as a function of SNS concentration for w/c ratios for 0.35 and 0.40 at 28 days of curing. These figures also compare the effect of the as-received and treated SNS flakes on the compressive strength of the cementitious composites. All cementitious composites reached their maximum compressive strength at a concentration of 0.2-wt%. The cementitious composites doped with the treated SNS flakes showed slightly higher compressive strength than those with the as-received SNS flakes. In addition, the cementitious composites with the w/c ratio of 0.35 showed higher compressive strength than those with the w/c ratio of 0.40. However, as shown in Fig. 4d, the cementitious composites with the w/c ratio of 0.4 exhibit slighter better percentage increase in the maximum compressive strength. At the w/c ratio of 0.35, the treated and as-received SNS flakes increased the compressive strength by as much as 11.51% and 8.35%, respectively, whereas at the w/c ratio of 0.4, the treated and as-received SNS flakes increased the compressive strength by as much as 13.24% and 9.94%, respectively. However, for all cementitious composites the improvement of the compressive strength diminished at 0.3-wt% SNS.

Fig. 5a-b show the effect of SNS on the splitting tensile strength of the cementitious composites at 28 days. The change in the tensile strength as a function of SNS concentration trend is similar to that of the compressive strength. For all cementitious composites, the addition of 0.2-wt% SNS yielded the highest tensile strength. This improvement is more noticeable for cementitious composites with the w/c ratio of 0.35 where the treated and as-received 0.2-wt% SNS enhanced the tensile strength by 37.6% and 33.3%, respectively (Fig. 5c). At the w/c ratio of 0.4, the 0.2-wt% treated and as-received SNS flakes improved the tensile strength by 32.8% and 31.2%, respectively (Fig. 5c). The enhancement of the tensile strength degraded at 0.3-wt% SNS.

3.3 Flexural properties

As depicted in Fig. 6a-b, the treated and as-received SNS flakes have somewhat different effects on the flexural strength. The flexural strength of the cementitious composites doped with the as-received SNS increased with SNS dosage, reaching its maximum at 0.2-wt%, then decreased at 0.3-wt%. On the other hand, the flexural strength of the cementitious composites doped with treated SNS is somewhat plateaued between 0.1-wt% and 0.2-wt% then decreased at 0.3-wt%. The treated SNS flakes seemed to outperform the as-received SNS flakes, presumably due to better dispersion. The cementitious composites with the w/c ratio of 0.35 exhibited a maximum flexural strength percentage increase of about 37.5% and 31.7% for treated and as-received SNS, respectively (Fig. 6c). When the w/c ratio is increased to 0.4, the treated and as-received SNS flakes improved the flexural strength by as much as 39.5% and 28.4%, respectively (Fig. 6c).

Fig. 7 shows the load-deflection responses of the cementitious composites. Overall, the addition of SNS improved the flexural behavior of the cementitious composites. The failure load, and flexural toughness and flexural modulus were all improved. The treated SNS flakes improved the flexural behavior of the cementitious composites with the w/c ratio of 0.35 more than the other cementitious composites. One noticeable enhancement is in the flexural modulus as shown in Fig. 8, Figs. 8a-b indicate that the flexural modulus increased with increasing SNS dosage. At the w/c ratio of 0.35, the cementitious composites with treated and as-received SNS flakes reached the same maximum flexural modulus at 0.2-wt%, yielding a percentage increase of about 32.69% (Fig. 8c). This percentage increase decreased at 0.3-wt% SNS (Fig. 8a). The flexural modulus of the cementitious composites containing treated SNS flakes with the w/c ratio of 0.4 increased at 0.1-wt% and remained constant at 0.2-wt%, then slightly decreased at 0.3-wt% (Fig. 8b). In this case, the treated SNS flakes increased the flexural modulus by as much as 30.6% (Fig. 8c). At the w/c ratio of 0.4, the as-received SNS flakes also improved the flexural modulus of the cementitious composites. A dosage of 0.2-wt% as-received SNS produced the same maximum flexural modulus as the treated 0.1-wt% and 0.2-wt% SNS (i.e., maximum percentage increase of 30.6%). However, the improvement of the flexural modulus significantly diminished at 0.3-wt% (Fig. 8b).

3.4 Fracture properties

The load-deflection responses of the notched prisms obtained from the three-point deflection tests are depicted in Fig. 9. The addition of treated and as-received SNS flakes enhanced the peak load and flexural modulus of the cementitious composites. The SNS flakes also increased the areas under the load-deflection curves and the maximum deflections (Fig. 9). In Fig. 10a-b, the fracture energy (G_F) of the cementitious composites is plotted against SNS concentration. As can be seen, the cementitious composites with the w/c ratio of 0.35 outperformed the cementitious composites with the w/c ratio of 0.4. At the w/c ratio of 0.35, G_F increased with increasing treated SNS dosage up to 0.2-wt% then dropped slightly at 0.3-wt%. Similarly, at this w/c ratio of 0.35, G_F increased with increasing as-received SNS dosage, followed by a significant drop at 0.3-wt%. As shown in Fig. 10c, at the w/c ratio of 0.35, the maximum percentage increase in G_F is 67.8% and 54.5% for treated and as-received SNS reinforced cementitious composites, respectively.

At the w/c ratio of 0.4, the addition of as-received SNS flakes increased G_F linearly up to 0.2-wt% then diminished at 0.3-wt% (Fig. 10c). The treated SNS flakes however increased G_F at 0.1-wt% after which their effect slowed and reached its maximum at 0.2-wt%. This enhancement also diminished at 0.3-wt%. The observed maximum percentage increase in G_F is 66.6% and 40.3% for treated and as-received SNS reinforced cementitious composites, respectively (Fig. 10c).

From Fig. 11, we can see that the enhancement of the fracture toughness (K_{IC}) somewhat follows the enhancement trend of G_F. All SNS reinforced cementitious composites reached their maximum K_{IC} at 0.2-wt% where for the cementitious composites with the w/c ratio of 0.35, the treated and as-received SNS flakes increased K_{IC} by 49.6% and 42.4%, respectively (Fig. 11c). At the w/c ratio of 0.4, the treated and as-received SNS flakes increased K_{IC} by 43.7% and 19.6%, respectively (Fig. 11c).

The enhancement of G_F and K_{IC} is reflected in the load-CMOD curves depicted in Fig. 12. As can be seen, all load-curves have similar shapes. The pre-peak slopes of the load-CMOD curves are similar. However, the SNS flakes increased the peak load in the load-CMOD curves of the cementitious composites, but they do not seem to affect the CMOD values at the peak loads. The post-cracking behavior of the cementitious composites with the w/c ratios of 0.35 is different from that of the cementitious composites with the w/c ratio of 0.4. At the w/c ratio of 0.35, the load decreased gradually while at the w/c ratio of 0.4, the load decreased somewhat rapidly (Fig. 12). This means, the area under the load-CMOD curves for the cementitious composites with the w/c of 0.35 is larger than that for the cementitious composites with the w/c ratio of 0.4, thus better post-cracking behavior. As depicted in Fig. 12a-b, the treated SNS flakes outperformed the as-received SNS flakes in enhancing the post-cracking behavior of the cementitious composites with the w/c ratio of 0.35. However, they slightly improved the post-cracking behavior of the cementitious composites with the w/c ratio of 0.4 (Fig. 12c-d).

3.5 Microstructure characterization

Fig. 13 illustrates XRD patterns and analysis of the cementitious composites containing 0 and 0.3-wt% SNS at the w/c ratio of 0.35 at 28 days. As can be seen from Fig. 13, the XRD pattern analysis revealed that the microstructure of the cementitious composites consists of alite (C_3S, COD 96-901-5085), ettringite (COD 96-901-5085), $Ca(OH)_2$ (COD 96-100-8782), calcite ($CaCO_3$, COD 96-900-9669) and carbonated calcium hemicarboaluminate (COD 96-210-5252).. The addition of SNS does not change the microstructure of the cementitious composites in term of hydration phases but it does alter the crystal diffraction peak intensities. The results of the Rietveld refinements shown in Fig. 13, demonstrate that the quantity of ettringite and $CaCO_3$ have increased from 8.4% and 21.3% to 15.6% and 31.4%, respectively. The amount of $Ca(OH)_2$ has decreased from 49.2% to 47.2%, while the content of alite and carbonated calcium hemicarboaluminate has decreased to 3.6% and 2.1%. It is well known that the intensity peaks corresponding to C-S-H phases are not detectable in the XRD patterns. However, the change in the C-S-H phases can be quantified by evaluating the change in the peak intensity of the other hydration phases such as $Ca(OH)_2$. As can be seen, the intensity peaks corresponding to ettringite and $CaCO_3$ increased with SNS dosage of 0.3-wt%. This means, the SNS flakes are effective in increasing C-S-H and other hydration phases especially for the cementitious composites infused with SNS.

Fig. 14 illustrates typical SEM images of the cementitious composites doped with treated SNS flakes at concentrations of 0.0, 0.1, 0.2 and 0.3-wt% at the w/c ratio of 0.35 at 28 days of curing. As depicted in Fig. 14a, the microstructure of the plain cement matrix is mainly composed of unhydrated cement particles, a small amount of calcium hydroxide (CH) and C-S-H. The microstructure also contains wide cracks (Fig. 14a), which can be attributed to the shrinkage. The addition of 0.1-wt% of treated SNS flakes increased the amount of the CH and C-S-H hydration phases and reduced crack propagation and crack width significantly (Fig. 14b-d). The addition of 0.2-wt% of treated SNS flakes further increased the amount of CH particles (Fig. 14c). These CH particles are in the form of hexagonal crystals that are uniformly distributed throughout the matrix. These CH crystals appear to be intercalated with the SNS flakes, thereby reducing shrinkage which resulted in a microstructure with fewer cracks and pores. We can also see from Fig. 14d that the inclusion of 0.3-wt% of treated SNS reduced the size of the CH crystals and produced CH/SNS agglomerates.

3.6 Discussion

The experimental results show that the SNS flakes are effective in improving the mechanical and fracture properties of the cementitious composites. Compared with graphene-based flakes, the SNS flakes are richer in hydroxyl functional groups thus they show good dispersibility in water. The workability of the cementitious pastes was not affected by the addition of the SNS flakes at 0.1 and 0.2-wt% dosages. However, the workability results suggest that higher SNS dosages reduce the workability of the cementitious composites. This could be attributed to the high specific surface area and high hydrophilicity of the SNS flakes. When used in high concentrations, SNS tends to absorb free water, thereby, increasing the internal friction between the cement particles which in turn reduces the workability of the cement pastes [24]. This trend was also observed in GO doped composites [50]. The SNS flakes improved the formation of the hydration phases of cement due to their high number of reactive functional groups. Because of this, the hydration kinetics in cementitious composites with SNS are superior to those in cementitious composites with graphene-based materials [27]. It appears that the addition of SNS altered the morphology of the cementitious composites. The SNS flakes regulated the microstructure by reducing cracks and creating denser microstructure with intercalated hexagonal CH/SNS particles.

Like graphene-based flakes, the SNS flakes improved the compressive strength of the composites. However, this improvement is moderate due to the restrictive properties of the cementitious materials when they are subjected to compressive stress. The observed maximum compression strength enhancement percentages are within the range of the percentages obtained from cementitious composites doped with graphene-based flakes. This means SNS and graphene-based materials have similar effects on the compressive strength of cementitious composites. The other mechanical properties such as splitting tensile and flexural strength, flexural modulus and fracture properties were also improved.

The tensile and flexure strength, flexural modulus and fracture properties of the cementitious composites were enhanced due to the inherent properties of the SNS flakes. These flakes have high specific surface area that contains many functional groups. These properties along with the SNS geometric features such as wrinkles and ripple enable the SNS flakes to form strong chemical and mechanical bonds with the hydration phases. This enhances the toughening and strengthening mechanisms induced by the SNS flakes in the cementitious composites. The strong interfacial bond between the SNS flakes and the hydration phases prevents the pull-out of the SNS flakes thereby linking them together to form a denser and packed microstructure with fewer cracks. Another important toughening mechanism induced by the SNS flakes is crack deflection. In this mechanism, cracks are deflected when the SNS flakes are present in their crack propagation paths. In this case, cracks find it hard to further propagate along their initial paths. As a result, they are delayed and then get deflected to regions without SNS flakes. This enables the cracks to take tortuous paths, thereby improves the flexural strength, flexural modulus, and fracture energy and fracture toughness of the cementitious composites as depicted in Fig. 6, Fig. 8, Fig. 10 and Fig. 11. The failure modes of the prisms subjected to four-point bending are given in Fig. 15. As can be seen, the plain prism (0-wt% SNS) failed in tension where the crack propagated straight from the bottom of the prism. However, for the cement prisms doped with the SNS flakes, zig-zag type-cracks were formed in the bottom side of the prisms due to the crack deflection mechanism, then propagated along their depths. As can be seen in Fig. 15, these tortuous crack propagation paths were formed with somewhat kick angles.

As expected, increasing the w/c ratio from 0.35 to 0.4 resulted in lower mechanical and fracture properties. The treated SNS flakes outperformed the as-received SNS flakes in improving the mechanical and fracture properties of the cementitious composites. However, the as-received SNS flakes produced acceptable percentage increases in these properties. This makes SNS flakes attractive for large-scale applications as they can be used in cementitious materials without treatment.

Even though the inherent mechanical properties of SNS are much lower than those of graphene-based materials, the obtained percentage increases in the compressive, tensile and flexural strength and fracture properties (including fracture properties) are within the range of the percentage increases obtained from cementitious composites doped with graphene-based materials [51]. This is significant because the cost and carbon footprint of SNS are much lower than those of graphene-based materials, thus making it a serious alternative reinforcing material in cementitious composites.

4. Conclusions

In this paper, we demonstrated that inexpensive and environmentally friendly biobased SNS flakes can improve the mechanical and fracture properties of cementitious materials. An extensive experimental program was carried to examine the performance of cementitious composites doped with treated and as-received SNS flakes using two w/c ratios. Based on the experimental results, the following main conclusions can be drawn:

- Owing to their high specific area and large number of reactive functional groups, the SNS flakes improved the hydration kinetics of the cementitious materials. These inherent properties along with their geometric features such as wrinkles and ripples seemed to improve the chemical and mechanical bonds between the SNS flakes and the hydration phases. This improved the engineering properties of the cementitious composites.
- The SNS flakes slightly improved the compressive strength of the cementitious composites, but they were more effective in increasing the tensile and flexural strength, flexural modulus, fracture energy and fracture toughness of the cementitious composites. This was due to the toughening mechanisms produced by SNS, mainly crack bridging and crack deflection.
- The SNS flakes produced percentage increases in mechanical and fracture properties similar to those produced by other competitor materials such as graphene and GO. This means SNS can be used as replacement for enhancing the performance of construction materials.
- Both treated and non-treated SNS present a new cost-effective and sustainable way for creating greener, stronger and durable construction materials that could have the potential of reducing the consumption and carbon footprint of OPC in the construction industry.

Acknowledgement

This research work is financially supported by the European Commission Horizon 2020 Marie Sklodowska-Curie Research Grant (B- SMART 799658) and the Scientific Research Foundation of Hunan provincial Education Department of China (22B0473). The authors are also grateful for the support from the National Natural Science Foundation of China (51878519).

Reference

[1] P.J.M. Monteiro, S.A. Miller, A. Horvath, Towards sustainable concrete, Nat. Mater. 16 (2017) 698–699.

[2] S.A. Miller, G. Habert, R.J. Myers, J.T. Harvey, Achieving net zero greenhouse gas emissions in the cement industry via value chain mitigation strategies, One Earth. 4 (2021) 1398–1411. https://doi.org/10.1016/j.oneear.2021.09.011.

[3] C. Zhou, J. Wang, X. Shao, L. Li, J. Sun, X. Wang, The feasibility of using ultra-high performance concrete (UHPC) to strengthen RC beams in torsion, J. Mater. Res. Technol. 24 (2023) 9961–9983. https://doi.org/10.1016/j.jmrt.2023.05.185.

[4] M. Hsie, C. Tu, P.S. Song, Mechanical properties of polypropylene hybrid fiber-reinforced concrete, Mater. Sci. Eng. A. 494 (2008) 153–157.

[5] P.S. Song, S. Hwang, Mechanical properties of high-strength steel fiber-reinforced concrete, Constr. Build. Mater. 18 (2004) 669–673.

[6] S. Wang, V.C. Li, Polyvinyl alcohol fiber reinforced engineered cementitious composites: material design and performances, in: Proc., Int'l Work. HPFRCC Struct. Appl. Hawaii, Citeseer, 2005.

[7] Y. Zhou, C.A. Orozco, E. Duque-Redondo, H. Manzano, G. Geng, P. Feng, P.J.M. Monteiro, C. Miao, Modification of poly (ethylene glycol) on the microstructure and mechanical properties of calcium silicate hydrates, Cem. Concr. Res. 115 (2019) 20–30.

[8] Z. Xiong, W. Wei, S. He, F. Liu, H. Luo, L. Li, Dynamic bond behaviour of fibre-wrapped basalt fibre-reinforced polymer bars embedded in sea sand and recycled aggregate concrete under high-strain rate pull-out tests, Constr. Build. Mater. 276 (2021) 122195. https://doi.org/10.1016/j.conbuildmat.2020.122195.

[9] C. Zhou, J. Wang, W. Jia, Z. Fang, Torsional behavior of ultra-high performance concrete (UHPC) rectangular beams without steel reinforcement: Experimental investigation and theoretical analysis, Compos. Struct. 299 (2022) 116022. https://doi.org/10.1016/j.compstruct.2022.116022.

[10] M.S.M. Norhasri, M.S. Hamidah, A.M. Fadzil, Applications of using nano material in concrete: A review, Constr. Build. Mater. 133 (2017) 91–97.

[11] M.S. Konsta-Gdoutos, Z.S. Metaxa, S.P. Shah, Highly dispersed carbon nanotube reinforced cement based materials, Cem. Concr. Res. 40 (2010) 1052–1059.

[12] M.M. Mokhtar, S.A. Abo-El-Enein, M.Y. Hassaan, M.S. Morsy, M.H. Khalil, Mechanical performance, pore structure and micro-structural characteristics of graphene oxide nano platelets reinforced cement, Constr. Build. Mater. 138 (2017) 333–339. https://doi.org/10.1016/j.conbuildmat.2017.02.021.

[13] S. Chuah, Z. Pan, J.G. Sanjayan, C.M. Wang, W.H. Duan, Nano reinforced cement and concrete composites and new perspective from graphene oxide, Constr. Build. Mater. 73 (2014) 113–124.

[14] B. Huang, J. Wang, G. Piukovics, N. Zabihi, J. Ye, M. Saafi, J. Ye, Hybrid cement composite-based sensor for in-situ chloride monitoring in concrete structures, Sensors Actuators B Chem. 385 (2023) 133638. https://doi.org/10.1016/j.snb.2023.133638.

[15] J. Sun, S. Lin, G. Zhang, Y. Sun, J. Zhang, C. Chen, A.M. Morsy, X. Wang, The effect of graphite and slag on electrical and mechanical properties of electrically conductive cementitious composites, Constr. Build. Mater. 281 (2021) 122606. https://doi.org/10.1016/j.conbuildmat.2021.122606.

[16] M. Murali, W.S. Alaloul, B.S. Mohammed, M.A. Musarat, M. Al Salaheen, A.M. Al-Sabaeei, A. Isyaka, Utilizing graphene oxide in cementitious composites: A systematic review, Case Stud. Constr. Mater. 17 (2022) e01359. https://doi.org/10.1016/j.cscm.2022.e01359.

[17] Y. Tang, Z. Huang, Z. Chen, M. Chen, H. Zhou, H. Zhang, J. Sun, Novel visual crack width measurement based on backbone double-scale features for improved detection automation, Eng. Struct. 274 (2023) 115158. https://doi.org/10.1016/j.engstruct.2022.115158.

[18] M.S. Soffian, F.Z. Abdul Halim, F. Aziz, M. A．Rahman, M.A. Mohamed Amin, D.N. Awang Chee, Carbon-based material derived from biomass waste for wastewater treatment, Environ. Adv. 9 (2022) 100259. https://doi.org/10.1016/j.envadv.2022.100259.

[19] Y. Gao, H. Jing, Z. Zhou, W. Chen, M. Du, Y. Du, Reinforced impermeability of cementitious composites using graphene oxide-carbon nanotube hybrid under different water-to-cement ratios, Constr. Build. Mater. 222 (2019) 610–621. https://doi.org/10.1016/j.conbuildmat.2019.06.186.

[20] R.K. Abu Al-Rub, B.M. Tyson, A. Yazdanbakhsh, Z. Grasley, Mechanical properties of nanocomposite cement incorporating surface-treated and untreated carbon nanotubes and carbon nanofibers, J. Nanomechanics Micromechanics. 2 (2012) 1–6.

[21] Y. Cao, P. Zavaterri, J. Youngblood, R. Moon, J. Weiss, The influence of cellulose nanocrystal additions on the performance of cement paste, Cem. Concr. Compos. 56 (2015) 73–83. https://doi.org/10.1016/j.cemconcomp.2014.11.008.

[22] M.Y. Xuan, X.Y. Wang, Multi-technique investigation regarding the impact of cellulose nanofibers on ultra-high-performance concrete at the macroscopic and microscopic levels, Constr. Build. Mater. 327 (2022) 126936. https://doi.org/10.1016/j.conbuildmat.2022.126936.

[23] S. Nassiri, Z. Chen, G. Jian, T. Zhong, M.M. Haider, H. Li, C. Fernandez, M. Sinclair, T. Varga, L.S. Fifield, M. Wolcott, Comparison of unique effects of two contrasting types of cellulose nanomaterials on setting time, rheology, and compressive strength of cement paste, Cem. Concr. Compos. 123 (2021) 104201. https://doi.org/10.1016/j.cemconcomp.2021.104201.

[24] H. Hasan, B. Huang, M. Saafi, J. Sun, Y. Chi, E. Whale, D. Hepworth, J. Ye, Novel engineered high performance sugar beetroot 2D nanoplatelet-cementitious composites, Constr. Build. Mater. 202 (2019) 546–562. https://doi.org/10.1016/j.conbuildmat.2019.01.019.

[25] B. Huang, Y. Chi, T. Almotlaq, J. Wang, M. Saafi, J. Ye, J. Sun, Y. Wang, J. Ye,

Influence of sugar beetroot microsheets on the hydration kinetics of cementitious composites : Electrochemical characterization, Cem. Concr. Compos. 144 (2023) 105314. https://doi.org/10.1016/j.cemconcomp.2023.105314.

[26] Y. Chi, B. Huang, M. Saafi, J. Ye, C. Lambert, Carrot-based covalently bonded saccharides as a new 2D material for healing defective calcium-silicate-hydrate in cement: Integrating atomistic computational simulation with experimental studies, Compos. Part B Eng. 199 (2020) 108235.

[27] Y. Chi, B. Huang, M. Saafi, N. Fullwood, C. Lambert, E. Whale, D. Hepworth, J. Ye, 2D bio-based nanomaterial as a green route to amplify the formation of hydrate phases of cement composites: Atomistic simulations and analytical characterization, Constr. Build. Mater. 299 (2021) 123867. https://doi.org/10.1016/j.conbuildmat.2021.123867.

[28] B.S. EN, 197-1: 2011 Cement, Compos. Specif. Conform. Criteria Common Cem. (2011).

[29] A. ASTM, C305-20. Standard practice for mechanical mixing of hydraulic cement pastes and mortars of plastic consistency, ASTM Int. (2020).

[30] P. Payakaniti, S. Pinitsoontorn, P. Thongbai, V. Amornkitbamrung, P. Chindaprasirt, Electrical conductivity and compressive strength of carbon fiber reinforced fly ash geopolymeric composites, Constr. Build. Mater. 135 (2017) 164–176. https://doi.org/10.1016/j.conbuildmat.2016.12.198.

[31] R. Dubey, P. Kumar, Effect of Fly Ash on Water/Powder Ratio and Superplasticizer Dosage in Self-Compacting Mortars, Int. J. Archit. Eng. Constr. (2013) 55–62. https://doi.org/10.7492/ijaec.2013.006.

[32] F. Collins, J. Lambert, W.H. Duan, The influences of admixtures on the dispersion, workability, and strength of carbon nanotube-OPC paste mixtures, Cem. Concr. Compos. 34 (2012) 201–207. https://doi.org/10.1016/j.cemconcomp.2011.09.013.

[33] I. Şanal, N. Özyurt Zihniołlu, A. Hosseini, Particle image velocimetry (PIV) to evaluate fresh and hardened state properties of self compacting fiber-reinforced cementitious composites (SC-FRCCs), Constr. Build. Mater. 78 (2015) 450–463. https://doi.org/10.1016/j.conbuildmat.2014.12.026.

[34] A. ASTM, Standard test method for compressive strength of hydraulic cement mortars (using 2-in. or [50-mm] cube specimens), Annu. B. ASTM Stand. B. ASTM Stand. 4 (2013) 1–9.

[35] B.S. 12390-2-2009 EN, Testing hardened concrete–Part 6: tensile splitting strength of test specimens, London Br. Stand. Inst. (2009).

[36] C. ASTM, Standard test method for flexural strength of concrete (using simple beam with third-point loading), in: Am. Soc. Test. Mater., 2010: pp. 12959–19428.

[37] D.R. RILEM, Determination of the fracture energy of mortar and concrete by means of three-point bend tests on notched beams, Mater. Struct. 18 (1985) 285–290.

[38] Y. Hu, D. Luo, P. Li, Q. Li, G. Sun, Fracture toughness enhancement of cement paste with multi-walled carbon nanotubes, Constr. Build. Mater. 70 (2014) 332–338.

[39] M. Sain, S. Panthapulakkal, Bioprocess preparation of wheat straw fibers and their characterization, Ind. Crops Prod. 23 (2006) 1–8.

[40] A. Kaushik, M. Singh, Isolation and characterization of cellulose nanofibrils from wheat straw using steam explosion coupled with high shear homogenization, Carbohydr. Res. 346 (2011) 76–85.

[41] A. Alemdar, M. Sain, Isolation and characterization of nanofibers from agricultural residues–Wheat straw and soy hulls, Bioresour. Technol. 99 (2008) 1664–1671.

[42] W. Chen, H. He, H. Zhu, M. Cheng, Y. Li, S. Wang, Thermo-responsive cellulose-based material with switchable wettability for controllable oil/water separation, Polymers (Basel). 10 (2018) 592.

[43] R.L. Oliveira, J.G. Vieira, H.S. Barud, R. Assunção, G. R Filho, S.J.L. Ribeiro, Y. Messadeqq, Synthesis and characterization of methylcellulose produced from bacterial cellulose under heterogeneous condition, J. Braz. Chem. Soc. 26 (2015) 1861–1870.

[44] B. Abderrahim, E. Abderrahman, A. Mohamed, T. Fatima, T. Abdesselam, O. Krim, Kinetic thermal degradation of cellulose, polybutylene succinate and a green composite: comparative study, World J. Environ. Eng. 3 (2015) 95–110.

[45] M. Li, L.J. Wang, D. Li, Y.L. Cheng, B. Adhikari, Preparation and characterization of cellulose nanofibers from de-pectinated sugar beet pulp, Carbohydr. Polym. 102 (2014) 136–143. https://doi.org/10.1016/j.carbpol.2013.11.021.

[46] J. Gong, J. Li, J. Xu, Z. Xiang, L. Mo, Research on cellulose nanocrystals produced from cellulose sources with various polymorphs, RSC Adv. 7 (2017) 33486–33493. https://doi.org/10.1039/c7ra06222b.

[47] K.S. Salem, N.K. Kasera, M.A. Rahman, H. Jameel, Y. Habibi, S.J. Eichhorn, A.D. French, L. Pal, L.A. Lucia, Comparison and assessment of methods for cellulose crystallinity determination, Chem. Soc. Rev. (2023) 6417–6446. https://doi.org/10.1039/d2cs00569g.

[48] G. Cheng, P. Varanasi, C. Li, H. Liu, Y.B. Melnichenko, B.A. Simmons, M.S. Kent, S. Singh, Transition of cellulose crystalline structure and surface morphology of biomass as a function of ionic liquid pretreatment and its relation to enzymatic hydrolysis, Biomacromolecules. 12 (2011) 933–941. https://doi.org/10.1021/bm101240z.

[49] H. Seddiqi, E. Oliaei, H. Honarkar, J. Jin, Cellulose and its derivatives : towards biomedical applications, Springer Netherlands, 2021. https://doi.org/10.1007/s10570-020-03674-w.

[50] X. Li, Y.M. Liu, W.G. Li, C.Y. Li, J.G. Sanjayan, W.H. Duan, Z. Li, Effects of graphene oxide agglomerates on workability, hydration, microstructure and compressive strength of cement paste, Constr. Build. Mater. 145 (2017) 402–410. https://doi.org/10.1016/j.conbuildmat.2017.04.058.

[51] Y. Suo, R. Guo, H. Xia, Y. Yang, B. Zhou, Z. Zhao, A review of graphene oxide/cement composites: Performance, functionality, mechanisms, and prospects, J. Build. Eng. 53 (2022) 104502. https://doi.org/10.1016/j.jobe.2022.104502.

Figures

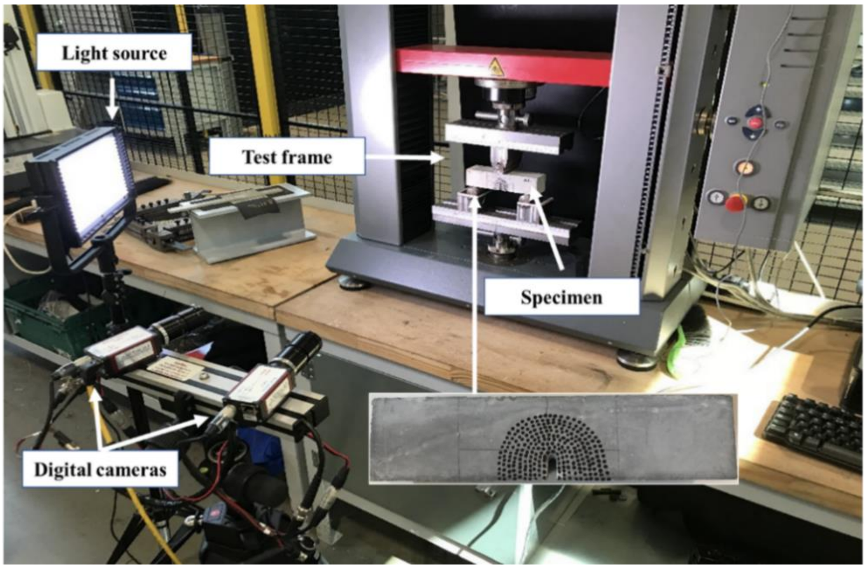

Fig. 1. Three-point bending setup with a video recording system for fracture tests.

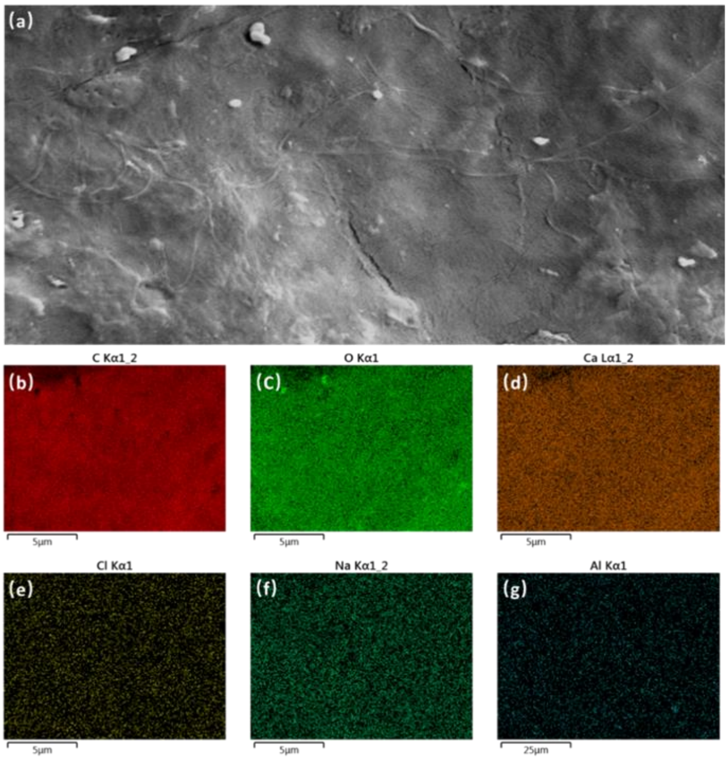

Chemical elements	O	C	Ca	Cl	Na	Al	Mg
Amount (%)	43.1	54.4	1.3	0.6	0.4	0.2	0.1

Fig. 2. SEM of SNS and EDX elemental mapping analysis of SNS (a) SEM image, (b) distribution of carbon element, (c) distribution of oxygen element, (d) distribution of calcium element, (e) distribution of chlorine element, (f) distribution of sodium, (g) distribution of aluminum element

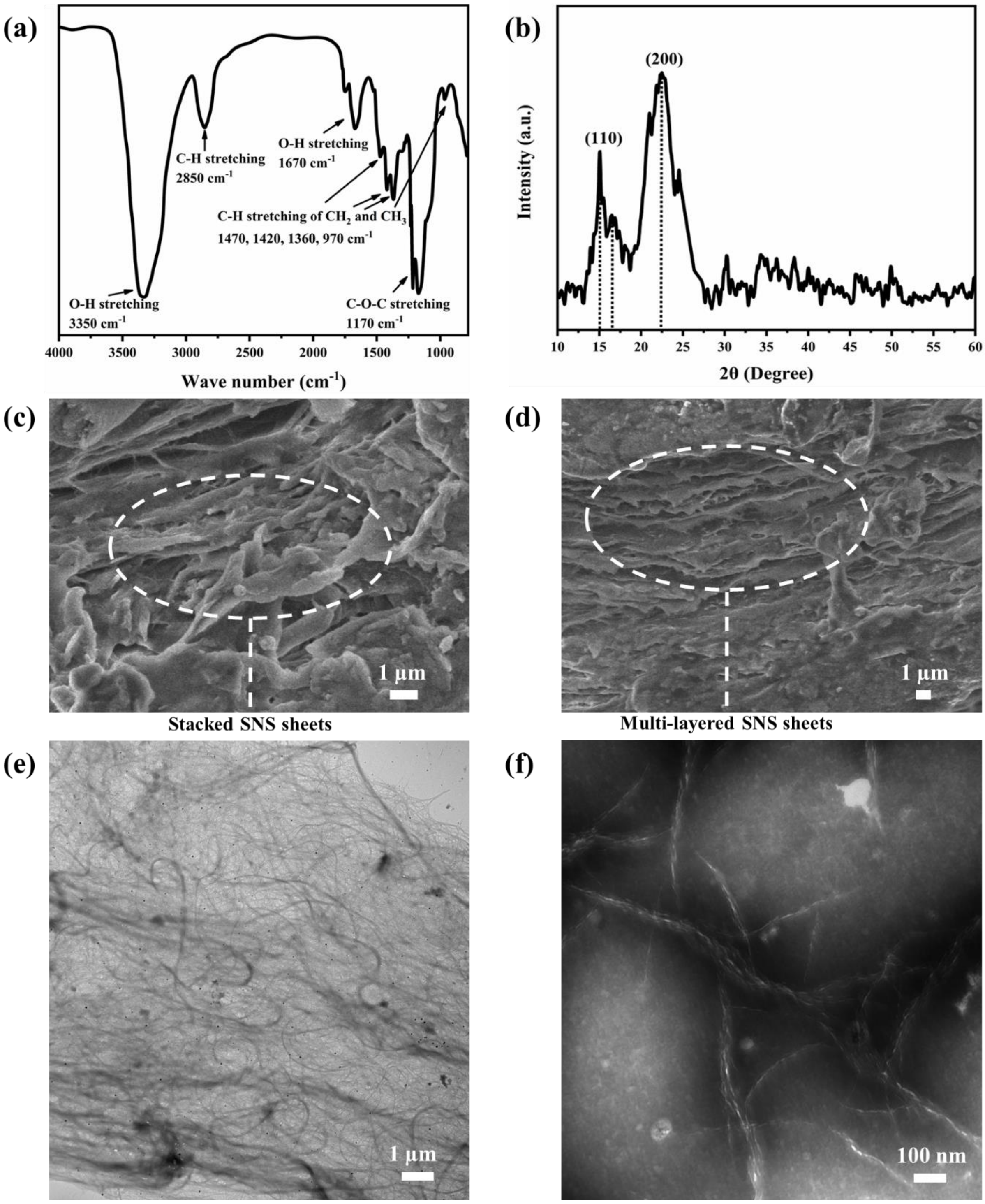

Fig. 3. Functional groups, crystal structure and morphology of SNS (a) FTIR spectrum, (b) XRD spectrum, (c-d) SEM images, (e-f) TEM images of SNS.

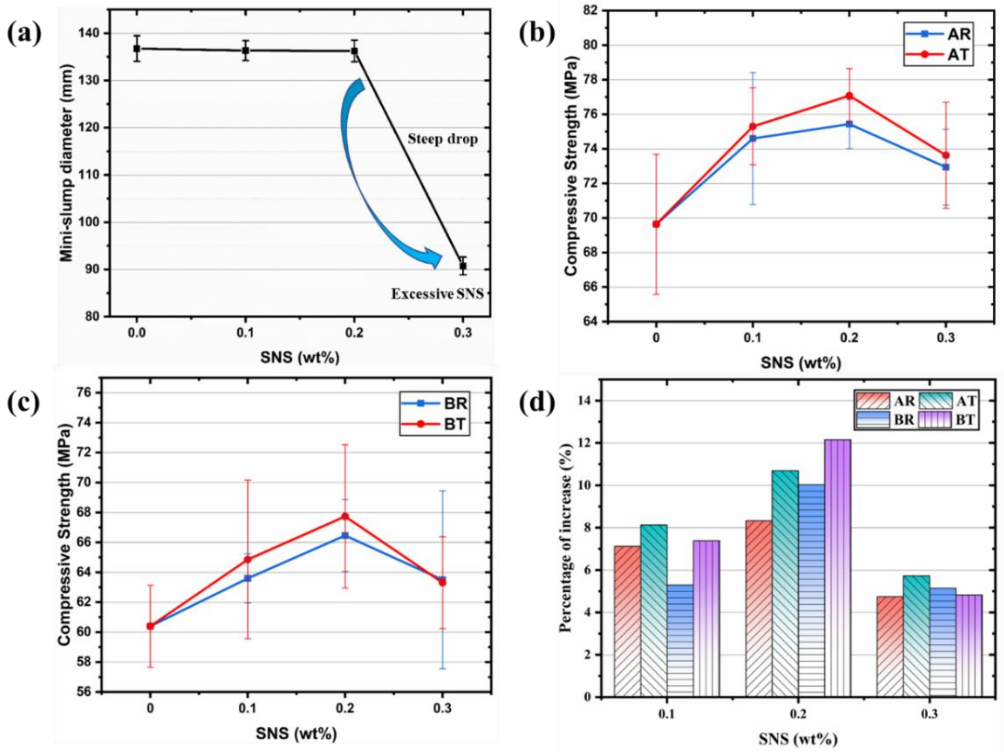

Fig. 4. Workability and compressive strength at 28 days (a) mini-slump workability, (b) compressive strength at a w/c ratio of 0.35, (c) compressive strength at a w/c ratio of 0.45, (d) percentage increases.

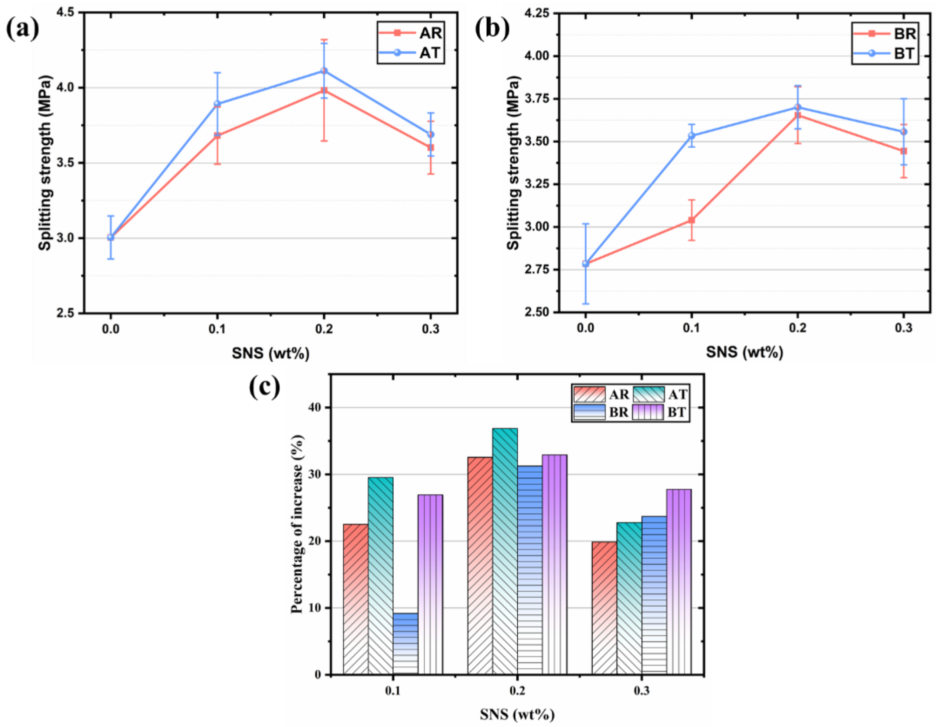

Fig. 5. Splitting tensile strength of cementitious composites at 28 days (a) as received and treated SNS with a w/c ratio of.35, (b) as received and treated SNS with a w/c ratio of 0.4, (c) percentage increases.

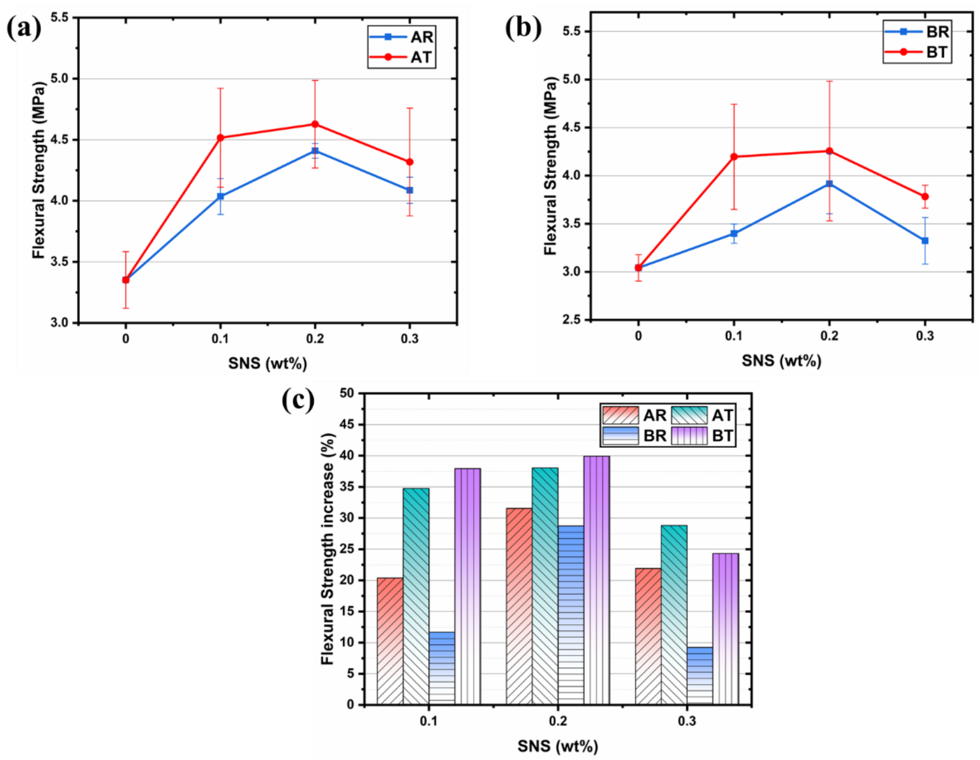

Fig. 6. Flexural strength of cementitious composites at 28 days (a) as received and treated SNS with a w/c of.35, (b) as received and treated SNS with a w/c of 0.4, (c) percentage increases.

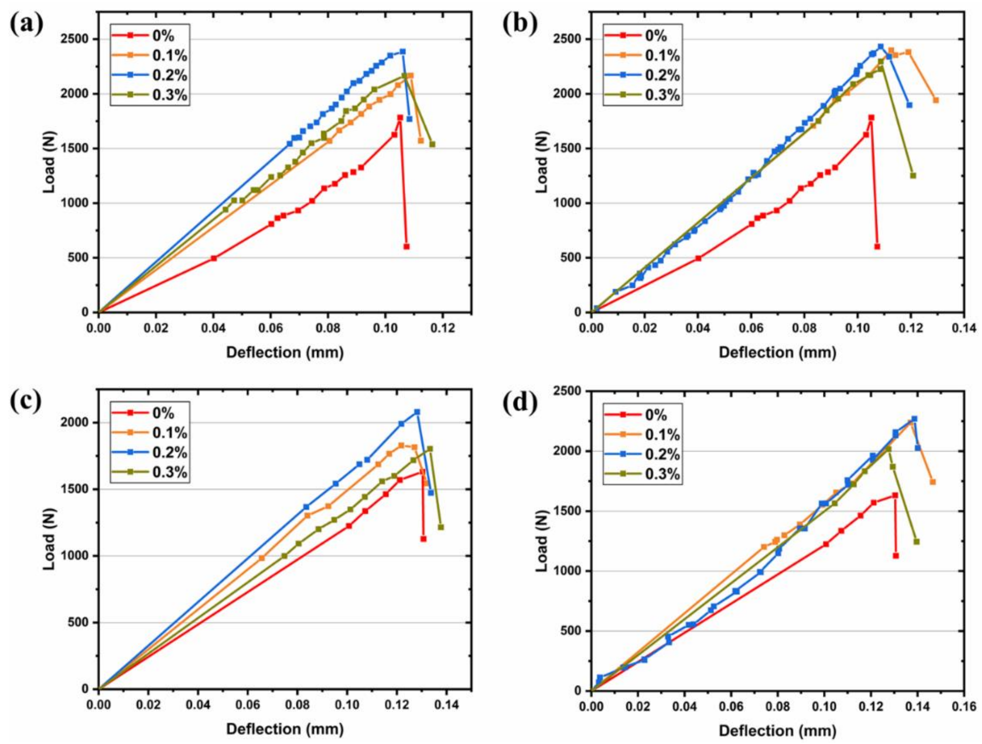

Fig. 7. Flexural load vs deflection curves of cementitious composites s at 28 days (a) as-received SNS with a w/c ratio of 0.35, (b) treated SNS with w/c ratio of 0.35, (c) as-received SNS with w/c ratio of 0.4, (d) treated SNS with a w/c ratio of 0.4.

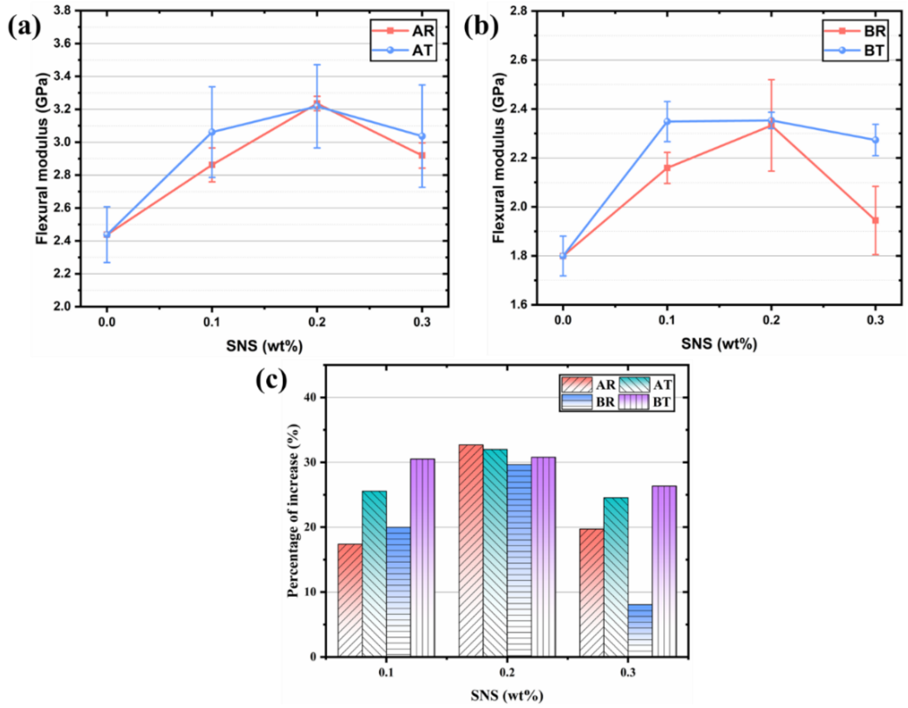

Fig. 8. Flexural modulus of cementitious composites at 28 days (a) as received and treated SNS with a w/c ratio of.35, (b) as received and treated SNS with a w/c ratio of 0.4, (c) percentage increases.

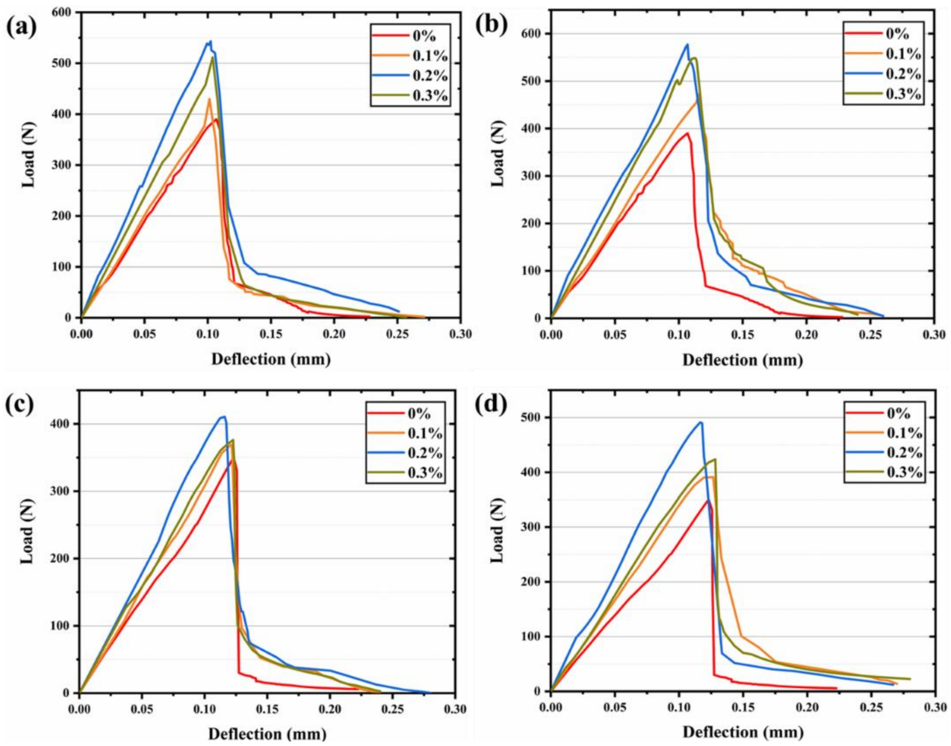

Fig. 9. P vs δ curves of cementitious composites at 28 days (a) as-received SNS with a w/c ratio of 0.35, (b) treated SNS with a w/c ratio of 0.35, (c) as-received SNS with a w/c ratio of 0.4, (d) treated SNS with a w/c of ratio 0.4.

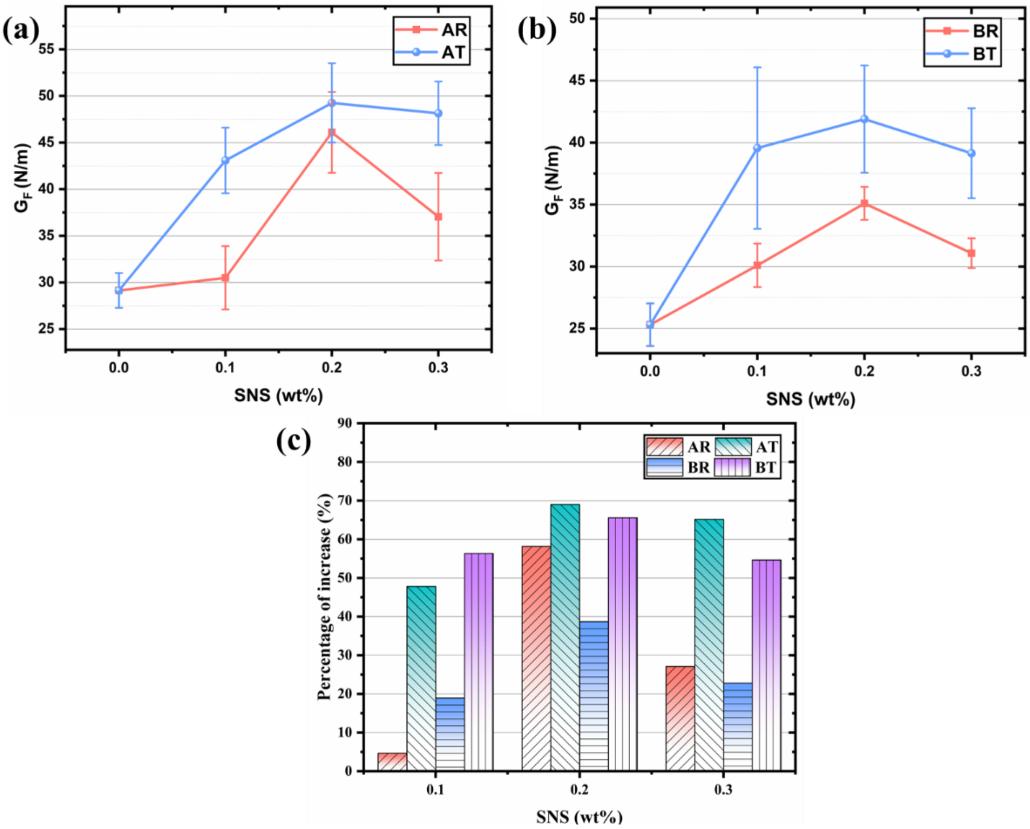

Fig. 10. Fracture energy at 28 days (a) with as received and treated SNS at a w/c of.35, (b) with as received and treated SNS at a w/c of 0.4, (c) percentage increases.

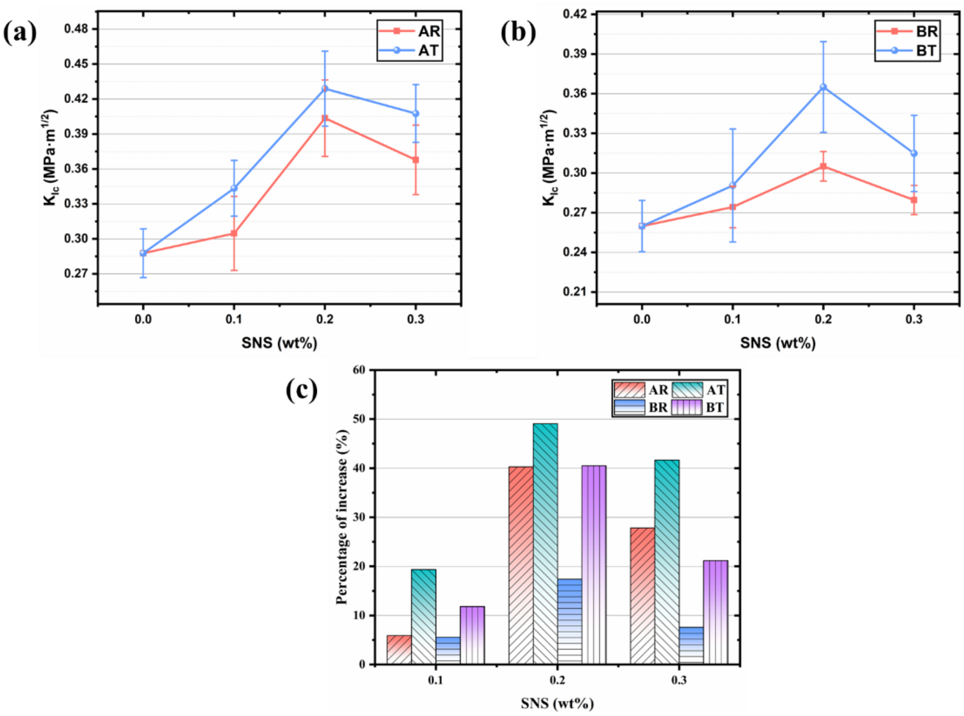

Fig. 11. Fracture toughness of cementitious composites at 28 days (a) as received and treated SNS with a w/c ratio of.35, (b) as received and treated SNS with a w/c ratio of 0.4, (c) percentage increases.

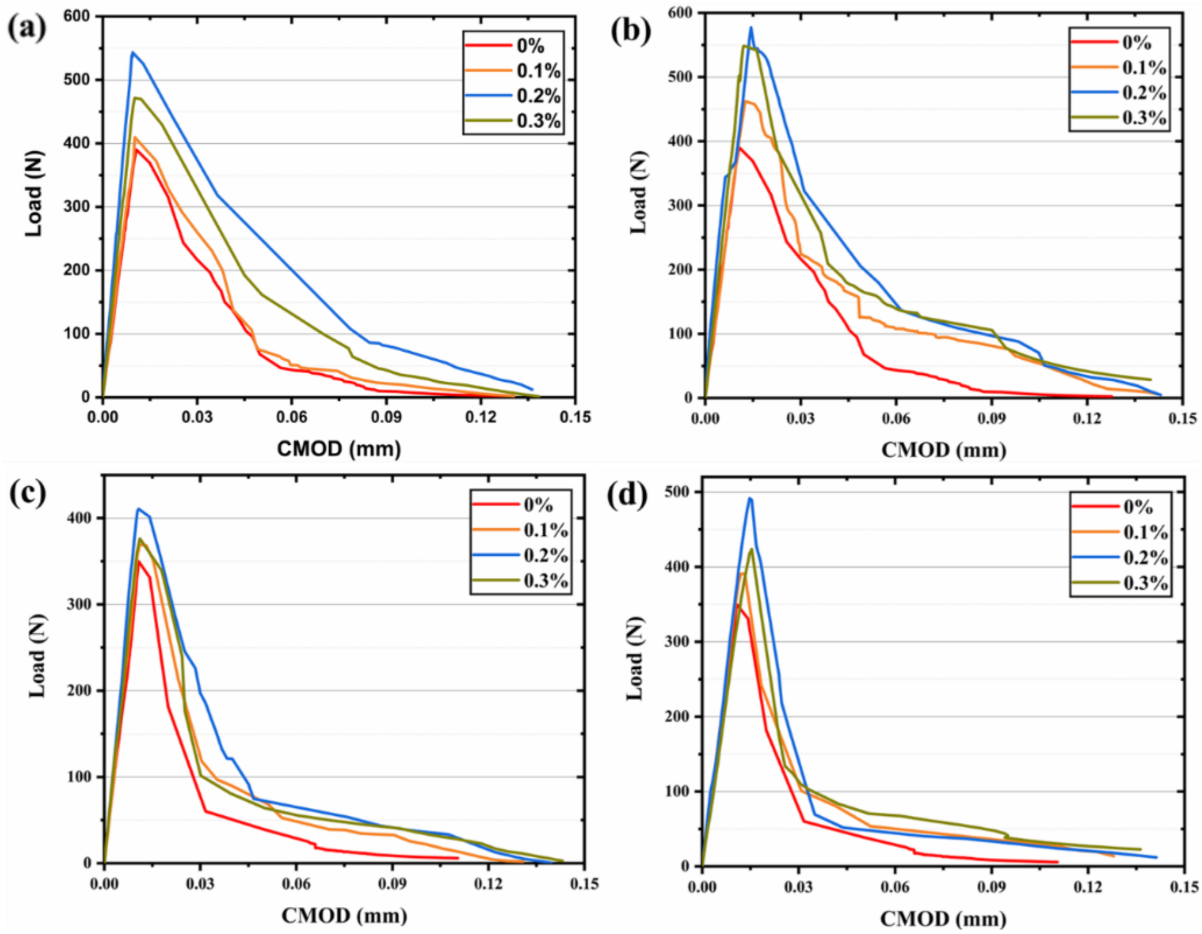

Fig. 12. Load-CMOD curves of cementitious composites. (a) as-received SNS with a w/c ratio of 0.35, (b) treated SNS with a w/c ratio of 0.35, (c) as-received SNS with a w/c ratio of 0.4, (d) treated SNS with a w/c of ratio 0.4

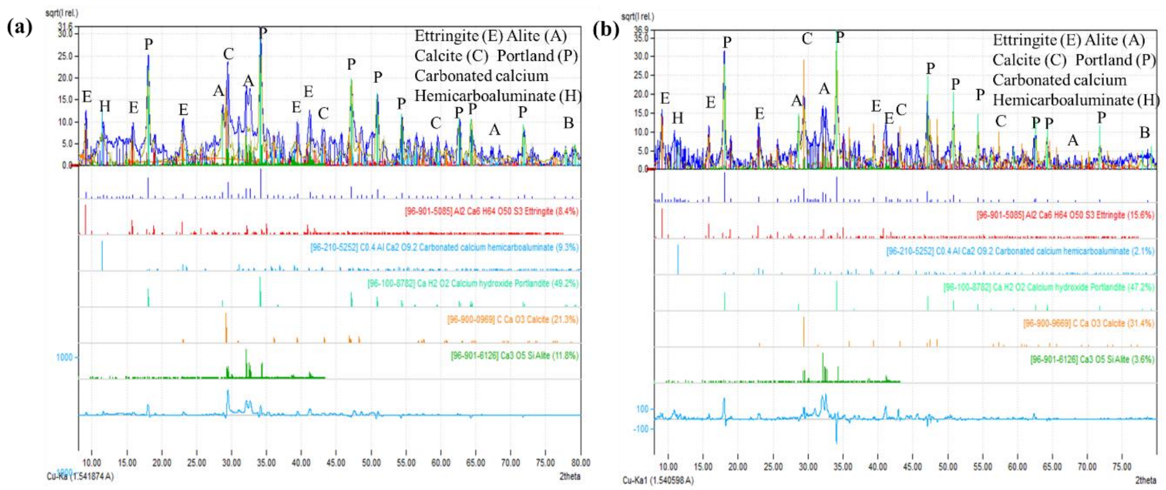

Fig. 13. XRD analysis of cementitious composites at 28 days (a) with 0 -wt% SNS, (b) with 0.3 -wt% SNS.

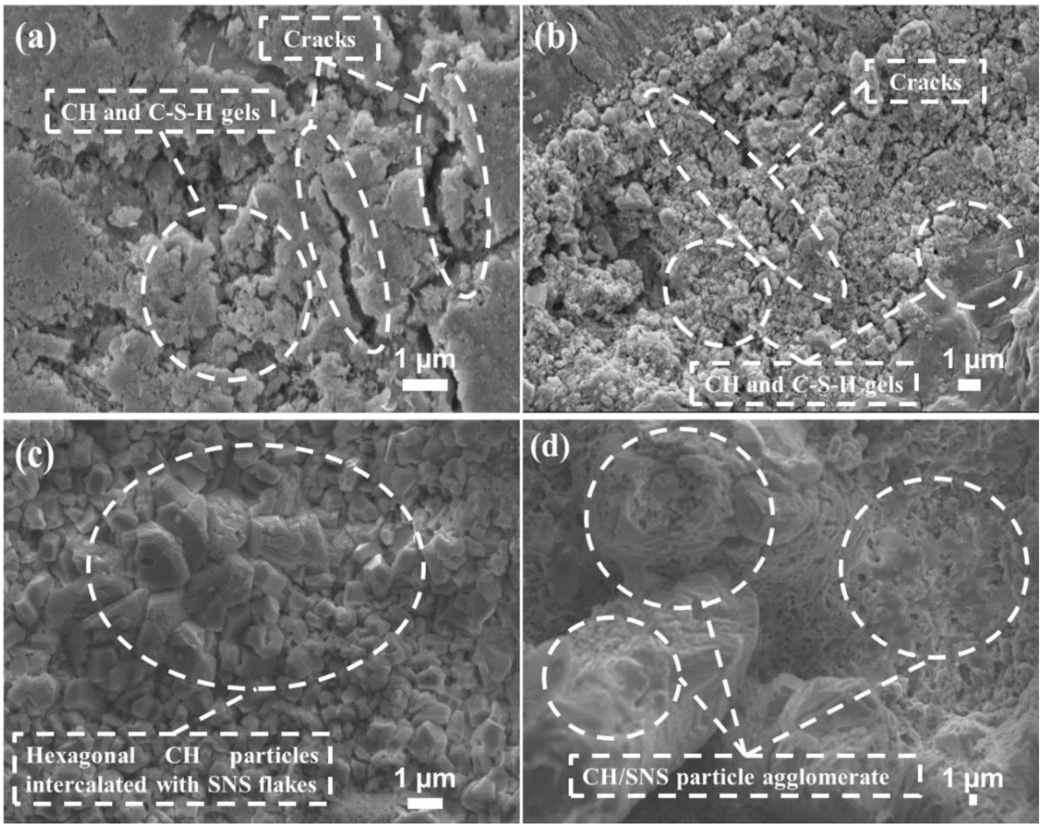

Fig. 14. SEM micro images of cementitious composites at 28 days (a) plain cementitious composite, (b) with 0.1-wt% treated SNS, (c) with 0.2-wt% treated SNS, (d) with 0.3-wt% treated SNS**.**

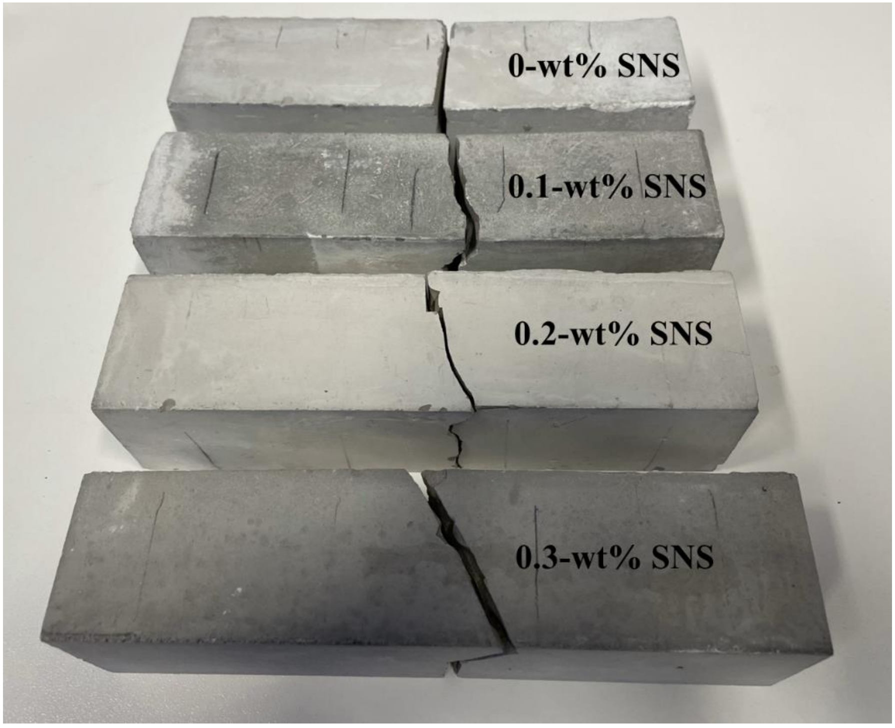

Fig. 15. Failure modes showing crack deflection mechanism in SNS reinforced cement prisms.

Tables

Table 1

Physical properties of OPC

Main particle size	pH	Relative density	Apparent density	Solubility in water
5-30 µm	11-13.5	2.75-3.20	0.9-1.5 g/cm³	Slight (0.1-1.5 g/l)

Table 2

Chemical components of OPC

Composition	SiO_2	Al_2O_3	Fe_2O_3	CaO	MgO	SO_3	K_2O	Na_2O	Cl
Amount (%)	20.85	5.22	2.25	64.98	2.40	3.37	0.61	0.27	0.05

Table 3

Mixture proportions of SNS platelet reinforced paste

Mix No.	Unit weight						
	Cement (g)	Water (g)	SP (g)	SNS(R) (g)	SNS(T) (g)	W/C ratio	SNS (wt%)
AP00	300	105.00	3	0.00	0.00	0.35	0.00
AR01	300	105.00	3	0.30	0.00	0.35	0.10
AR02	300	105.00	3	0.60	0.00	0.35	0.20
AR03	300	105.00	3	0.90	0.00	0.35	0.30
AT01	300	105.00	3	0.00	0.30	0.35	0.10
AT02	300	105.00	3	0.00	0.60	0.35	0.20
AT03	300	105.00	3	0.00	0.90	0.35	0.30
BP00	300	105.00	3	0.00	0.00	0.40	0.00
BR01	300	105.00	3	0.30	0.00	0.40	0.10
BR02	300	105.00	3	0.60	0.00	0.40	0.20
BR03	300	105.00	3	0.90	0.00	0.40	0.30
BT01	300	105.00	3	0.00	0.30	0.40	0.10
BT02	300	105.00	3	0.00	0.60	0.40	0.20
BT03	300	105.00	3	0.00	0.90	0.40	0.30

P: plain cement, R: as-received SNS and T: treated SNS.

Declaration of interests

☒The authors declare that they have no known competing financial interests or personal relationships that could have appeared to influence the work reported in this paper.

☐The authors declare the following financial interests/personal relationships which may be considered as potential competing interests: